Biosensors and Bioelectronics 64 (2015) 311–317

Contents lists available at ScienceDirect

Biosensors and Bioelectronics

journal homepage: www.elsevier.com/locate/bios

A plasmon-assisted fluoro-immunoassay using gold nanoparticle-decorated carbon nanotubes for monitoring the influenza virus

Jaewook Lee [a,e], Syed Rahin Ahmed [b,c], Sangjin Oh [c], Jeonghyo Kim [c], Tetsuro Suzuki [d], Kaushik Parmar [e], Simon S. Park [e], Jaebeom Lee [c,*], Enoch Y. Park [a,b,**]

[a] Research Institute of Green Science and Technology, Shizuoka University, 836 Ohya Suruga-ku, Shizuoka 422-8529, Japan
[b] Department of Bioscience, Graduate School of Science and Technology, Shizuoka University, 836 Ohya Suruga-ku, Shizuoka 422-8529, Japan
[c] Department of Nano Fusion and Cogno-Mechatronics Engineering, Pusan National University, Busan 609-735, Republic of Korea
[d] Department of Infectious Diseases, Hamamatsu University School of Medicine, 1-20-1 Higashi-ku, Handa-yama, Hamamatsu 431-3192, Japan
[e] Department of Mechanical and Manufacturing Engineering, University of Calgary, Calgary, Canada, T2N 1N4

ARTICLE INFO

Article history:
Received 1 August 2014
Received in revised form
3 September 2014
Accepted 6 September 2014
Available online 16 September 2014

Keywords:
Plasmon-assisted fluoro-immunoassay
Gold nanoparticle-decorated carbon nanotube
CdTe quantum dot
Influenza virus detection platform
Plasmonic resonance energy transfer

ABSTRACT

A plasmon-assisted fluoro-immunoassay (PAFI) was developed for the detection of the influenza virus by using Au nanoparticle (Au NP)-decorated carbon nanotubes (AuCNTs) that were synthesized using phytochemical composites at room temperature in deionized water. Specific antibodies (Abs) against the influenza virus were conjugated onto the surface of AuCNTs and cadmium telluride quantum dots (QDs), which had a photoluminescence intensity that varied as a function of virus concentration and a detection limit of 0.1 pg/mL for all three types of influenza viruses examined. The clinically isolated influenza viruses (A/Yokohama/110/2009 (H3N2)) were detected in the range of 50–10,000 PFU/mL, with a detection limit of 50 PFU/mL. From a series of proof-of-concept and clinical experiments, the developed PAFI biosensing system provided robust signal production and enhancement, as well as an excellent selectivity and sensitivity for influenza viruses. This nanoparticle-based technique could be potentially developed as an efficient detection platform for the influenza virus.

1. Introduction

Many kinds of nanomaterials have been recently used in the area of nanobiotechnology research. The unique physicochemical properties of nanomaterials have found a significant number of applications in biosensing, imaging, and drug delivery system (Ahmed et al., 2013; Lee et al., 2014; Leung et al., 2012; Li and Mezzenga, 2013; Wang et al., 2013b). In particular, nanobiosensing systems have gained popularity owing to its high sensitivity, selectivity, and rapid response time (Liu et al., 2012; Yin et al., 2013). The detection techniques used in various nanobiosensing applications include magnetophoresis, electrochemical analysis, plasmonic coupling immunoassays, and fluoro-immunoassays (Draz et al., 2012; Kim et al., 2013; Li et al., 2013; Viet et al., 2013; Zhou et al., 2012, 2013). The plasmon-assisted fluoro-immunoassay (PAFI) has been used to analyze specific biomaterials (Ahmed et al., 2014; Li et al., 2012; Nooney et al., 2010; Sharma et al., 2013b). The PAFI is based on the plasmonic resonance energy transfer (PRET) phenomenon, which causes a photoluminescence (PL) enhancement from the interactions between the plasmonic nanomaterials and the semiconductor nanoparticles (Lee et al., 2004, 2005, 2007). Such hybrid structures can be used to detect the interaction between an antibody (Ab) and its antigen, because of their tuned optical properties. Although numerous plasmonic nanomaterials have been introduced (*e.g.*, gold, silver, platinum, and metal NPs), Au NP-decorated carbon nanotubes (AuCNTs) have received considerable attention, owing to their unique properties. Au NPs are able to exhibit surface plasmon resonance (Jana et al., 2001; Lee et al., 2011b). Carbon nanotubes exhibit electroconductivity and harbor many π electrons on their surfaces (Jariwala et al., 2013; Sun et al., 2011). Thus, AuCNTs are expected to show a synergistic effect owing to their roles as biosensing platforms, signal enhancers, and signal transducers (McAndrew and

* Corresponding author.
** Corresponding author at: Shizuoka University, Research Institute of Green Science and Technology, 836 Ohya Suruga-ku, Shizuoka 422-8529, Japan.
E-mail addresses: jaebeom@pusan.ac.kr (J. Lee), acypark@ipc.shizuoka.ac.jp (E.Y. Park).

http://dx.doi.org/10.1016/j.bios.2014.09.021
0956-5663/

Baxendale, 2013; Sharma et al., 2013a; Wang et al., 2013a; Yick et al., 2013).

Combining the above mentioned heterogeneous materials requires sophisticated strategies in order to conserve carbon nanotube (CNT) structures and to bind two materials without the help of organic bridges. One of the well-known processes for preparing AuCNT nanostructures involves reduction with chemical reducing agents such as sodium borohydride or hydrazine (Yu et al., 2014; Zhang et al., 2013). An alternative process involves thiol- or amine-assisted interactions between Au NPs and CNT surfaces (Georgakilas et al., 2007; Li et al., 2011). Attachment of Au NPs onto CNT surfaces has been attempted using the processes of electrodeposition, DNA hybridization, and chemical reaction (Georgakilas et al., 2007; Gobbo et al., 2013; Li et al., 2011; Li and Cooper-White, 2013; Peng et al., 2009). However, these approaches can cause CNT damage and organic/biological electric resistance, which may adversely affect their electrical and mechanical properties (Hirsch, 2002; Holzinger et al., 2001).

In this study, we suggest a novel and easy method for preparing AuCNTs by using phytochemicals. The synthetic reaction was carried out in deionized (DI) water at room temperature *via* sonication and stirring processes, without resorting to external heating or application of high pressure. No electrochemistry equipment was used in the above procedure. AuCNTs were produced as follows. Au ions were first attached onto the surface of CNTs and they were then reduced to Au NPs on the CNT surface. This process was catalyzed using a mixture of gallic acid and isoflavone phytochemicals, two well-known natural antioxidants (Aruoma et al., 1993; Park et al., 2009) that served as mild reducing agents (Lee et al., 2011a). Furthermore, the generated AuCNTs were applied onto the influenza virus detection platform by using a quantum dot (QDs)-assisted PAFI.

In this study, we developed a PAFI-based detection platform for the influenza virus, using antibody-conjugated AuCNTs and CdTe QDs. In all, we tested three types of influenza viruses, *viz.* the Influenza virus A/Beijing/262/95 (H1N1), the Influenza virus/New Caledonia/20/99IvR116 (H1N1), and the clinically isolated Influenza virus A/Yokohama/110/2009 (H3N2). The minimum detection limit for the influenza virus was 0.1 pg/mL. The clinically isolated influenza virus was also monitored in the range 50–10,000 PFU/mL, with a detection limit of 50 PFU/mL. Our virus detection platform would be immensely useful not only for detecting the influenza virus, but also for detecting various other viruses and viral diseases.

2. Material and methods

2.1. Materials and instruments

$HAuCl_4 \cdot 3H_2O$, multi-walled carbon nanotubes (MWCNTs), gallic acid, EDC, NHS, cadmium perchlorate hydrate, and cysteamine were purchased from Sigma-Aldrich (Milwaukee, WI, USA). Aluminum telluride (Al_2Te_3) was obtained from the Cerac Company (Milwaukee, WI, USA). The isoflavone was isolated from commercial soybeans. 3,3′,5,5′-tetramethylbenzidine was purchased from Dojindo (Osaka, Japan). The ECL™ anti-mouse IgG, horseradish peroxidase (HRP)-conjugated whole antibody (Ab) was obtained from GE Healthcare UK, Ltd. (Buckinghamshire, UK). Goat anti-rabbit IgG-HRP was purchased from Santa Cruz Biotechnology, Inc. (Santa Cruz, CA, USA). Anti-Influenza A virus hemagglutinin (HA) Ab Ab66189, which is a mouse monoclonal antibody [B219M] for the influenza A virus HA H1 and positive against influenza virus A/Beijing/262/95 (H1N1), A/New Caledonia/20/99 (H1N1), and A/Taiwan/1/86 (H1N1), was purchased from Abcam Inc. (Cambridge, UK). Anti-neuraminidase (NA) (New Caledonia/20/1999/(H1N1)), a rabbit polyclonal Ab, was obtained from Immune Technology Corp. (New York, NY, USA). Anti-H3 (H3N2) (Ab82454), a mouse monoclonal Ab [InA227] to H3 (H3N2) that recognizes influenza virus A HA H3, was purchased from Abcam Inc. (Cambridge, UK). Influenza virus New Caledonia/20/99IvR116 (H1N1) and A/Beijing/262/95 (H1N1) were purchased from Sino Biological Inc. (Beijing, China) and HyTest Lyd (Turku, Finland), respectively. Influenza virus A/Yokohama/110/2009 (H3N2) was isolated from a clinically isolated sample, which was kindly provided by Dr. C. Kawakami of Yokohama City Institute of Health, Japan and was used to assess the versatility of this assay system.

The absorbance of AuCNTs and the corresponding PL enhancement were measured using a filter-based multimode microplate reader (Infinite® F500, TECAN, Ltd., Männedorf, Switzerland), and the chemical reactions and surface functional groups were monitored by FT-IR spectroscopy (FT-IR 6300, JASCO, Corp. Tokyo, Japan). The morphologies and sizes of the nanostructures were characterized by TEM (JEM-2100F, JEOL, Ltd., Tokyo, Japan). An X-ray powder diffractometer (RINT ULTIMA, Rigaku, Corp., Tokyo, Japan) was used to characterize AuCNT by using CuKa radiation and a Ni filter. The data were collected from 2 theta=0–100° at a scan rate of 0.01° per step and 10 s per point. The AuCNTs and MWCNTs were analyzed by Raman spectroscopy (HR-800, Lab-RAM, HORIBA Ltd., Kyoto, Japan). In order to measure the electroconductivity, AuCNT solution was dropped on the planar interdigitated electrode (planar IDE-Pt/0.25″, Synkera, USA) and dried at room temperature. Then, the current change of the deposited area was monitored by linear sweep voltammetry from −1 V to 1 V (SP-150, BioLogic, France). A plate reader (Model 680, Bio-Rad, Hercules, USA) was used to confirm the presence of Ab-conjugated nanomaterials. The PL image of the hybrid nanostructure was observed using a confocal laser-scanning microscope (LSM 700, Carl Zeiss Microimaging, GmbH, Göttingen, Germany).

2.2. Synthesis of AuCNTs and CdTe QDs

AuCNTs were synthesized at room temperature by using commercially available reagents. Forty milligrams of MWCNT was dispersed in 100 mL of nitric acid and boiled for 5 h to prepare the hydrophilic MWCNTs. Subsequently, 0.01 mmol of $HAuCl_4 \cdot 3H_2O$ and 2 mg of acid-treated MWCNTs were dispersed in 30 mL of DI water by sonication for 30 min. Subsequently, 600 μL of GI solution was added into the MWCNT/Au ion solution, and then stirred vigorously for 1 h. The GI solution was used as a reducing agent and stabilizer, and prepared as follows: 10 mg of isoflavone was dissolved in 10 mL of the 0.01 M gallic acid solution. The cysteamine-coated CdTe QDs were synthesized as reported in detail elsewhere (Gaponik et al., 2002; Lee et al., 2010).

2.3. Preparation of antibody-conjugated AuCNTs and CdTe QDs

In order to conjugate the Abs to the AuCNTs, amine-functionalized AuCNTs and Ab-conjugated EDC/NHS were prepared. To modify the surface of the Au NPs, 1 mg of AuCNTs was dispersed in 10 mL of DI water. Then, 1 mL of 0.01 M cysteamine was added into the AuCNT solution. After 30 min of stirring, this mixture was centrifuged to separate the amine-functionalized AuCNTs. Additionally, 100 μL of the 4 mM EDC and 10 mM NHS were added in the 96-well plate and incubated and gently shaken for 30 min at 200 rpm with 1 μL of anti-HA Ab (Ab66189) (final concentration of 5 ng/mL) for the EDC/NHS coupling reaction. Finally, 30 μL of the amine-functionalized AuCNT (1 μg/μL) and activated anti-HA Ab (Ab66189) were mixed in all wells and shaken for 3 h for effective bioconjugation. Anti-NA (New Caledonia/20/1999/(H1N1)) and anti-HA (Ab82454) Abs were also conjugated to the surfaces of the Au CNTs by using the same procedure. Anti-HA (Ab66189) and

anti-HA (Ab82454)-conjugated CdTe QDs were also prepared by using the procedure for Ab-conjugated AuCNTs.

2.4. Plasmon assisted fluoro-immunoassay (PAFI) for influenza virus detection

In order to detect the influenza virus *via* PAFI, 45 μL of Ab-conjugated AuCNTs and 45 μL of the CdTe QDs were mixed in each of the 96 wells. Consequently, serially diluted influenza virus was added into each well and shaken for 1 h. During this process, the Ab-conjugated AuCNTs and the CdTe QDs were found to bind each other in the presence of the influenza virus, owing to the affinity between the antigen on the surface of virus and its corresponding antibody. To evaluate the efficacy of PAFI as a detection platform, the following three types of influenza viruses were used: A/Beijing/262/95 (H1N1), New Caledonia/20/99IvR116 (H1N1), and A/Yokohama/110/2009 (H3N2). The PL intensities were measured as a function of the concentration of the influenza virus. The PAFI was carried out at an excitation wavelength of 380 nm, and the excitation and the emission slits were 5 and 10 nm in width, respectively. The PL intensity of this system was monitored at 518 nm during signal detection. In order to evaluate the PAFI system with different influenza virus, all detection experiment was carried out over 3 times.

3. Results and discussion

3.1. Design and preparation of AuCNTs for PAFI

The synthesis of AuCNTs comprised two steps (Fig. 1), *viz.* the preparation of plasmonic nanomaterials (step I), and the processing of PAFI for influenza virus detection by using AuCNTs and QDs (step II). Firstly, the acid-treated multi-walled CNTs (MWCNTs) were dispersed in DI water containing a gold precursor (Au^{3+}) by using sonication. Owing to the π-electrons and oxygen moieties on the surface of the acid-treated MWCNTs, Au^{3+} is able to attach onto the surface of MWCNTs through electrostatic attraction. In order to decorate Au NPs onto the MWCNTs, the Au ions were reduced to Au NPs, using a mixture of gallic acid and isoflavone (GI solution). AuCNTs were obtained after 1 h of stirring and washing with DI water. To perform the PAFI for influenza virus detection by using AuCNTs, anti-hemagglutinin (HA) Ab or anti-neuraminidase (NA) Ab specific for the influenza virus were conjugated onto the surfaces of AuCNTs and QDs by using a *N*-ethyl-*N*′-(dimethylaminopropyl) carbodiimide (EDC)/*N*-hydroxysuccinimide (NHS)-coupling reaction (step II in Fig. 1). In the presence of the influenza virus, the distance between the Ab-conjugated AuCNTs and the QDs diminishes by an affinity between an antigen and its Ab. Depending on the concentration of the influenza virus, the formation of the AuCNT and QD hybrid structures caused a variation in the PL intensities. In the PAFI system, plasmonic material is not single Au NP but AuCNT assembly structure. Thus the energy transfer to enhance the PL property would be taken a place at the sandwich structure between plasmonic AuCNT structure and fluorescent CdTe QDs with virus. Moreover, this sandwich structure could lead the PL enhancement through the collective effect between plasmonic materials and fluorescent nanoparticles (Lee et al., 2004).

3.2. Morphology of AuCNTs

In order to confirm the decoration of Au NPs onto MWCNTs, the morphology of MWCNTs and AuCNTs were examined using transmission electron microscopy (TEM). The MWCNTs showed the presence of a slick surface that was over 3 μm in length (Figs. 2A and S1A, respectively). However, after two steps of the decoration reaction, a large number of Au NPs were detected on the surface of MWCNTs (Figs. 2B and S1B). The carbon structure of MWCNT is transparent, but as heavy metals show high electron absorption, Au NPs are easily distinguishable in the TEM images. The average particle size of the Au NPs was 20 nm, and they were

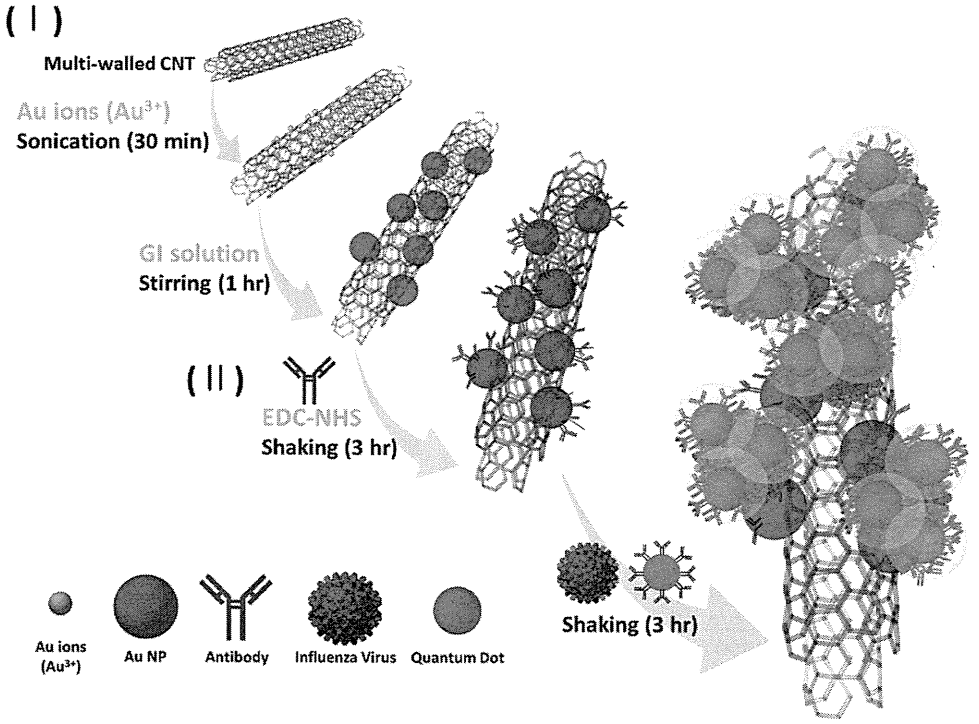

Fig. 1. (I) Synthetic scheme for the preparation of Au nanoparticle (NP)-decorated CNT nanostructures (AuCNTs) and (II) the process of influenza virus detection by using PAFI, non-scalable.

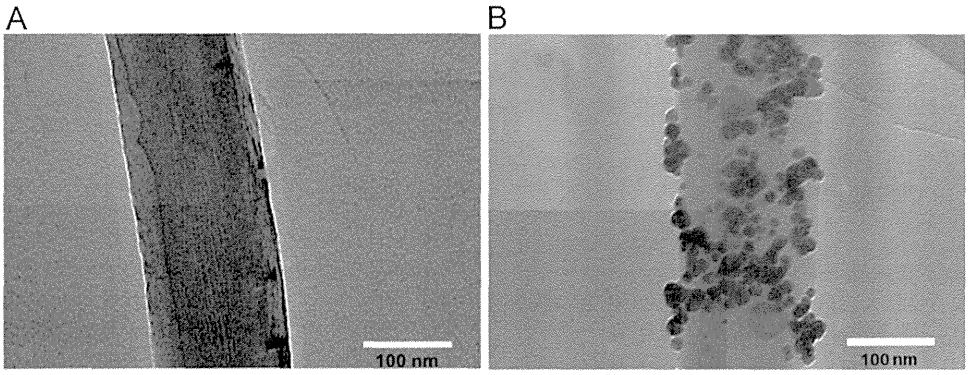

Fig. 2. TEM images of (A) MWCNTs and (B) AuCNTs.

well dispersed with a high density over the large surface area of the MWCNTs (Fig. S1B).

3.3. *Optical, surface-enhanced Raman scattering, physicochemical, and electrical properties of AuCNTs*

The optical absorbance of AuCNTs was measured using a filter-based absorbance-mode microplate reader. Typically, the plasmon peak of Au NPs that are 20 nm in radius occurs at 525 nm. However, the surface plasmonic absorbance of Au NPs was observed as a black spectrum at 550 nm (Fig. 3A), and its bands were broadened and non-symmetric; however, large-sized (> 50 nm) particles were not observed in the corresponding TEM image. Plasmon-coupling between adjacent Au NPs might have occurred, owing to the delocalized π-electron cloud on the surface of MWCNTs. This interaction caused a broadened and non-symmetric plasmonic band of Au NPs. Thus MWCNT can play a role as mediator for plasmonic coupling interaction, thus optical property of this hybrid structure could be enhanced (Lee et al., 2012). However, in the MWCNT case, the specific absorbance as plasmonic peak was not observed by UV/vis spectroscopy. Thus, only MWCNT was not suitable for PAFI detection platform. The structural characteristics of the AuCNTs were elucidated based on the powder X-ray diffraction (XRD) pattern (Fig. 3B). A strong diffraction peak corresponding to the 002 plane of the MWCNTs was presented at 2 theta=26.2° in the XRD pattern (ICSD card no: 01-075-1621). Meanwhile, several new diffraction patterns and weak carbon peaks were measured in the AuCNTs (Fig. 3B, red pattern). The presence of Au NPs in the nanostructure was confirmed by the characteristic diffraction peaks from the face-centered cubic packing arrangement of bulk Au *i.e.*, the (111), (200), (220), (311), (222), and (400) planes at 2 theta values of 38.2°, 44.4°, 64.6°, 77.5°, 81.7°, and 98.1° (ICSD card no: 00-004-0784), respectively. Au NPs possess a higher crystallinity than the carbon structures, because of the metal NPs. Thus, the diffraction patterns of Au NPs were stronger than those of the carbon face. The surface-enhanced Raman scattering (SERS) was measured by Raman spectroscopy at the excitation wavelength of 514 nm (Fig. 3C). The peak at 1340 cm^{-1} indicates that the D band occurred due to the local disorder present in the AuCNT structure

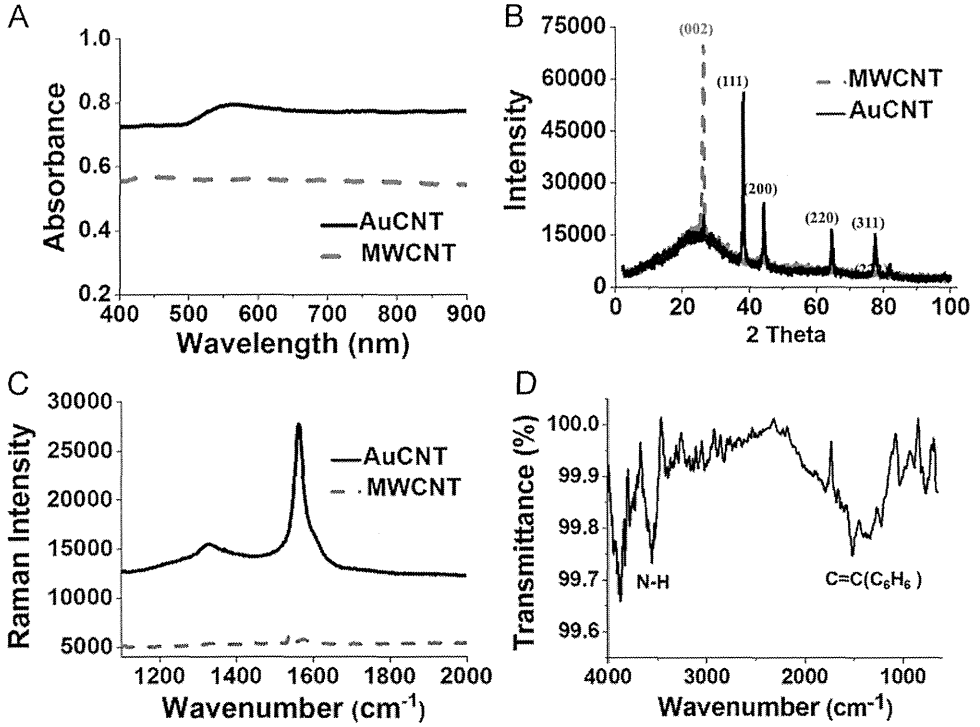

Fig. 3. Physicochemical properties of the AuCNTs. (A) UV/vis spectra, (B) XRD data, (C) Raman spectra of MWCNT with Au ions (red dash line) and AuCNTs (black line), and (D) FT-IR spectra of the amine-functionalized AuCNTs. (For interpretation of the references to color in this figure legend, the reader is referred to the web version of this article.)

(Sharma et al., 2013a). In addition, a G peak appeared near 1580 cm^{-1}, which is related to the characteristic feature (especially to the sp^2-hybridized carbon allotropes) of the graphitic layers (Baro et al., 2013). As expected, the Raman spectrum intensity was more enhanced in the AuCNTs than in the MWCNTs (Sharma et al., 2013a) The spectrum intensity of AuCNTs was 5 times higher than that of MWCNTs. Therefore, the SERS effect was induced by decoration of Au NPs onto the MWCNT surface. The functional group of the amine-functionalized AuCNT was analyzed using Fourier Transform Infrared (FT-IR) spectroscopy. For the EDC/NHS coupling reaction with the carboxylic group of the influenza virus antibody, the N-H vibration of AuCNT was detected around 1250 cm^{-1} and 3400–3500 cm^{-1} (Fig. 3D), respectively. These bands around 1450–1580 cm^{-1} are characteristic of the aromatic bonds of MWCNT. The C–O single-bond vibration was observed at 1010 cm^{-1}. The electroconductivities of the AuCNTs and MWCNTs were measured using a finger type Pt electrode *via* the linear sweep method. The average linear resistance of AuCNT was approximately 0.007 mΩ, whereas that of MWCNT was much higher (Fig. S2). From these physicochemical results, it was evident that the AuCNT composite exhibits enhanced properties such as SERS and electrical conductivity. Furthermore, we could experimentally establish the fact that critical damage to the AuCNT structure indeed did not occur, and that AuNPs were directly attached onto the surface of the CNTs, owing to a mild reduction reaction.

3.4. *PAFI performance for influenza virus detection by using AuCNT*

In order to assess the PAFI performance for the influenza virus detection, three types of antibodies, *viz.* anti-HA (H1) (Ab66189), anti-neuraminidase (NA) (New Caledonia/20/1999/(H1N1)), and anti-HA (H3N2) (Ab82454) were conjugated onto the surface of AuCNTs (step II in Fig. 1). In addition, the surfaces of CdTe QDs were also conjugated with anti-HA (H1) (Ab66189) and anti-HA (H3N2) (Ab82454) antibodies by using the same method. In this case, the Ab-conjugated AuCNTs play the role of plasmon-supplying substrates, whereas the Ab-conjugated CdTe QDs act as PL-monitoring materials. Prior to virus detection, conjugation of the Abs to the AuCNTs or CdTe QDs was verified using an ELISA (Fig. S3). Anti-HA (Ab66189) and anti-NA (New Caledonia/20/1999/ (H1N1))-conjugated AuCNTs, and anti-HA (Ab66189)-conjugated CdTe QDs displayed strong signals (Fig. S3A, B, and C, respectively). In the case of the anti-HA (Ab82454)-conjugated AuCNTs and the CdTe QDs, the recorded absorbance was lower than that of the other Ab-conjugated NPs (Fig. S4). These results indicate that all antibodies were successfully conjugated onto the surface of the AuCNTs and the CdTe NPs.

The Ab-conjugated nanostructures were used for constructing the PAFI system. The detection of the influenza virus was made possible by using a confocal laser-scanning microscope (Fig. 4). Influenza virus A/Beijing/262/95 (H1N1) was dosed into the anti-HA Ab-conjugated AuCNTs and onto the CdTe system. In the presence of the virus, the distance between the HA Ab-conjugated AuCNTs and the HA Ab-conjugated CdTe QDs was reduced, owing to the affinity between the antigen on the surface of the virus and conjugated antibody. Subsequently, the hybrid nanowire structure showed green PL (Fig. 4D–F). However, no PL was observed at all in the absence of the virus (Fig. 4A–C).

In addition, the sensitivity of the PAFI was demonstrated with two different influenza viruses; A/Beijing/262/95 (H1N1) and New Caledonia/20/99IvR116 (H1N1), respectively. All procedures were

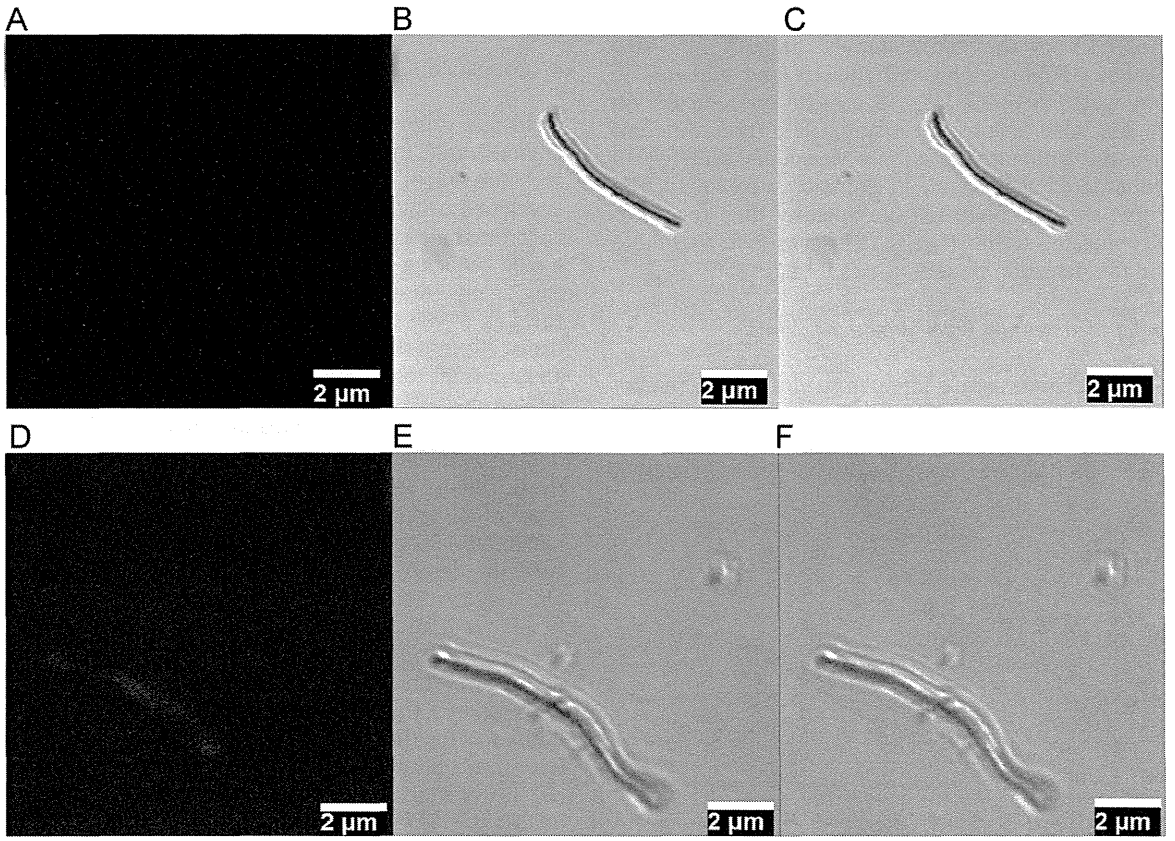

Fig. 4. Confocal laser-scanning microscopy images of the AuCNT-QD hybrid structure obtained *via* the anti-HA Ab conjugation reaction with influenza virus A/Beijing/262/95 (H1N1). (A)–(C) Before and (D)–(F) after the conjugation reaction with influenza virus. (A) and (D) are fluorescent images; (B) and (E) are DIC images; (C) and (F) are merged images.

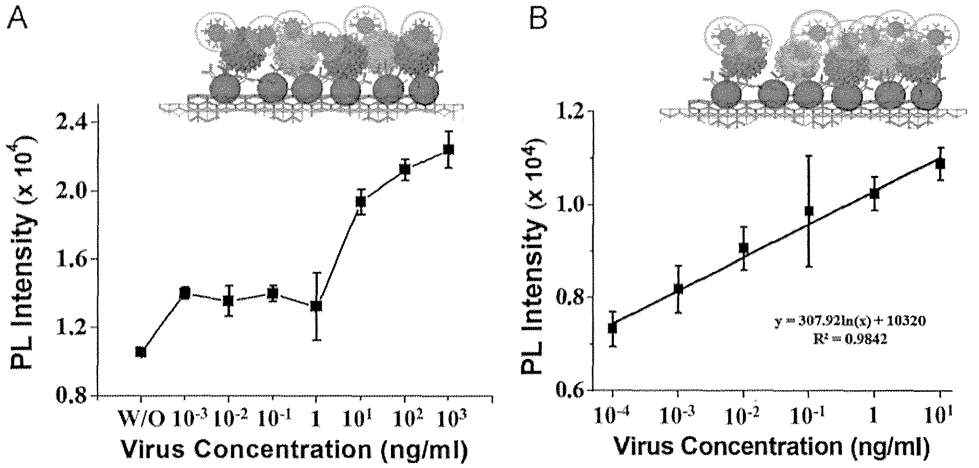

Fig. 5. The calibration curve of the PL intensity corresponding to the concentration of (A) Influenza virus A/Beijing/262/95 (H1N1) and (B) Influenza virus/New Caledonia/20/99IvR116 (H1N1). (For interpretation of the references to color in this figure, the reader is referred to the web version of this article.)

carried out in a 96-well plate. As the concentration of the influenza virus was increased, the PL intensity corresponding to both of the viruses also increased (Fig. S5). This implies that the binding affinity between the Ab-conjugated AuCNTs and the CdTe QDs was dependent on the virus concentration. Furthermore, using anti-HA Ab (Ab66189)-conjugated AuCNTs and CdTe QDs, we carried out the PAFI for the influenza virus A/Beijing/262/95 (H1N1). The detection was carried out at 518 nm, and a calibration curve corresponding to the virus concentrations was obtained (Fig. 5A). In this case, the detection limit was 1 ng/mL. As the same antibody was conjugated onto the surface of both the nanomaterials, a binding competition took place between the Ab-conjugated AuCNTs and the CdTe QDs against virus. To improve the detection limit of PAFI, various different antibodies were conjugated onto the surface of each of the nanomaterials: anti-NA Ab (New Caledonia/20/1999/(H1N1))-conjugated AuCNTs and anti-HA Ab (Ab66189)-conjugated CdTe QDs (Fig. 5B, anti-NA Ab; red color Ab and anti-HA Ab; blue color Ab). Using these two different nanostructures the influenza virus/New Caledonia/20/99IvR116 (H1N1) was monitored at the same PL emission wavelength. The calibration curve shows a more reliable linearity than that with the same Ab-conjugated system (Fig. 5B). The sensitivity was more improved, and the detection limitation was 0.1 pg/mL.

3.5. Detection of the clinically isolated influenza virus

The clinically isolated sample (influenza virus A/Yokohama/110/2009 (H3N2)) was also detected by PAFI using the anti-HA Ab (Ab82454)-conjugated AuCNTs and CdTe QDs at 518 nm in the 96-well plate. The PL intensity was dramatically changed as a function of the virus concentration. In the presence of the influenza virus, the PL intensity showed an 8-fold increase, as compared to the corresponding intensity in the absence of the same virus (Fig. S6). The calibration curve was obtained in the range 50–10,000 PFU/mL (Fig. 6) and the detection limit was 50 PFU/mL. This implies that the clinically isolated virus was successfully detected by PAFI using the Ab-conjugated AuCNTs and the CdTe QDs. The selectivity of PAFI was confirmed using the anti-HA Ab (Ab66189)-conjugated AuCNTs and the CdTe QDs. The anti-HA Ab (Ab66189) could only recognize the HA present in the influenza virus (H1N1). The PL for influenza virus A/Yokohama/110/2009 (H3N2) was low, similar to that of the negative control (BSA) (Fig. S7).

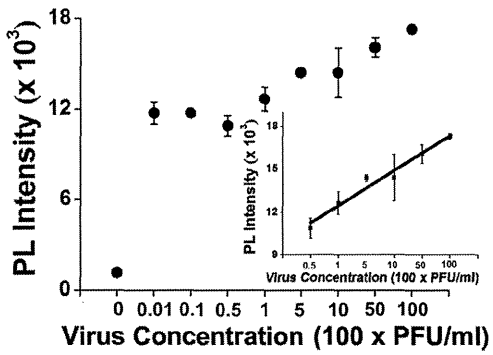

Fig. 6. The calibration curve of the clinically isolated influenza virus A/Yokohama/110/2009 (H3N2).

4. Conclusion

In this study, the influenza virus monitoring was successfully demonstrated by interaction between plasmonic nanomaterials and fluorescent particles. In particular, novel PAFI system was developed using AuCNT and CdTe nanomaterials. To perform the PAFI, the AuCNTs were prepared by a simple 2 step-process, using a mild reducing agent without thermal assistance or harsh reducing agents. A large number of Au NPs were decorated onto the surfaces of the CNTs, and they showed a surface plasmon resonance effect at the AuCNT surface. Thus, the AuCNT surface played an important role as the plasmonic substrate for the PAFI. Various influenza viruses were monitored and the detection limits of PAFI against influenza viruses A/Beijing/262/95 (H1N1) and New Caledonia/20/99IvR116 (H1N1) were 1 ng/mL and 0.1 pg/mL, respectively. For the detection of the New Caledonia virus, two different types of antibodies were attached onto the surface of each of the nanomaterials, and then used for monitoring the virus. In this case, the detection limitation was higher than that of the single antibody system (Beijing virus detection), owing to less competitive binding affinity. In previous reports, the detection limitation for proteins and viruses was reported to be approximately in the ng range (Ahmed et al., 2014; Li et al., 2012; Nooney et al., 2010). As compared to the other PAFI detection systems, the detection limitation for this particular system was improved by about 10-fold. The clinically isolated influenza virus A/Yokohama/110/2009 (H3N2) was also tested, and the corresponding sensitivity was 50 PFU/mL. The PAFI system also showed excellent selectivity, which was 100-fold higher than that of the commercial diagnostic kit. This system may be applied not only to the influenza virus, but also to various other infectious viruses.

Acknowledgment

We wish to thank Dr. C. Kawakami of the Yokohama City Institute of Health, Japan for providing the influenza virus A/Yokohama/110/2009 (H3N2). This work was supported partly by the Promotion of Nanobio-technology Research to support Aging and Welfare Society from the Ministry of Education, Culture, Sports, Science and Technology, Japan. This study was supported by a grant from the Korean Health Technology R&D Project, Ministry of Health & Welfare, Republic of Korea (HI13C0862); and by the Basic Science Research Program through the National Research Foundation of Korea (NRF), funded by the Ministry of Education, Science and Technology (2013004637).

Appendix A. Supplementary information

Supplementary data associated with this article can be found in the online version at http://dx.doi.org/10.1016/j.bios.2014.09.021.

References

Ahmed, S.R., Dong, J.H., Yui, M., Kato, T., Lee, J., Park, E.Y., 2013. J. Nanobiotechnol. 11, 28.
Ahmed, R.S., Hossain, M.A., Youn Park, J., Kim, S.H., Lee, D., Suzuki, T., Lee, J., Park, E. Y., 2014. Biosens. Bioelectron. 58, 33–39.
Aruoma, O.I., Murcia, A., Butler, J., Halliwell, B., 1993. J. Agric Food Chem. 41, 1880–1885.
Baro, M., Nayak, P., Baby, T.T., Ramaprabhu, S., 2013. J. Mater. Chem. A 1, 482–486.
Draz, M.S., Fang, B.A., Li, L.J., Chen, Z., Wang, Y.J., Xu, Y.H., Yang, J., Killeen, K., Chen, F. F., 2012. ACS Nano 6, 7634–7643.
Gaponik, N., Talapin, D.V., Rogach, A.L., Hoppe, K., Shevchenko, E.V., Kornowski, A., Eychmuller, A., Weller, H., 2002. J. Phys. Chem. B 106, 7177–7185.
Georgakilas, V., Gournis, D., Tzitzios, V., Pasquato, L., Guldi, D.M., Prato, M., 2007. J. Mater. Chem. 17, 2679–2694.
Gobbo, P., Biesinger, M.C., Workentin, M.S., 2013. Chem. Commun. 49, 2831–2833.
Hirsch, A., 2002. Angew. Chem. Int. Ed. 41, 1853–1859.
Holzinger, M., Vostrowsky, O., Hirsch, A., Hennrich, F., Kappes, M., Weiss, R., Jellen, F., 2001. Angew. Chem. Int. Ed. 40, 4002.
Jana, N.R., Gearheart, L., Murphy, C.J., 2001. Langmuir 17, 6782–6786.
Jariwala, D., Sangwan, V.K., Lauhon, L.J., Marks, T.J., Hersam, M.C., 2013. Chem. Soc. Rev. 42, 2824–2860.
Kim, J., Lee, J., Lee, K.I., Park, T.J., Kim, H.J., Lee, J., 2013. Sens. Actuators B: Chem. 177, 327–333.
Lee, J., Govorov, A.O., Dulka, J., Kotov, N.A., 2004. Nano Lett. 4, 2323–2330.
Lee, J., Govorov, A.O., Kotov, N.A., 2005. Angew. Chem. Int. Ed. 44, 7439–7442.
Lee, J., Hernandez, P., Lee, J., Govorov, A.O., Kotov, N.A., 2007. Nat. Mater. 6, 291–295.
Lee, J., Kim, H.Y., Zhou, H., Hwang, S., Koh, K., Han, D.W., Lee, J., 2011a. J. Mater. Chem. 21, 13316–13326.
Lee, J., Orazbayev, A., Govorov, A.O., Kotov, N.A., 2010. J. Phys. Chem. C 114, 1404–1410.
Lee, J., Park, E., Lee, J., 2014. Bioprocess Biosyst. Eng. 37, 983–989.
Lee, J., Zhou, H., Lee, J., 2011b. J. Mater. Chem. 21, 16935–16942.
Lee, Y.H., Polavarapu, L., Gao, N., Yuan, P., Xu, Q.H., 2012. Langmuir 28, 321–326.
Leung, K.C.F., Xuan, S.H., Zhu, X.M., Wang, D.W., Chak, C.P., Lee, S.F., Ho, W.K.W., Chung, B.C.T., 2012. Chem. Soc. Rev. 41, 1911–1928.
Li, C.X., Mezzenga, R., 2013. Nanoscale 5, 6207–6218.
Li, H., Chen, C.Y., Wei, X., Qiang, W.B., Li, Z.H., Cheng, Q., Xu, D.K., 2012. Anal. Chem. 84, 8656–8662.
Li, H.Q., Cooper-White, J.J., 2013. Nanoscale 5, 2915–2920.
Li, X.L., Qin, Y.J., Picraux, S.T., Guo, Z.X., 2011. J. Mater. Chem. 21, 7527–7547.
Li, Y.X., Hong, M., Qiu, B., Lin, Z.Y., Cai, Z.W., Chenb, Y.T., Chen, G.N., 2013. Chem. Commun. 49, 10563–10565.
Liu, Y.X., Dong, X.C., Chen, P., 2012. Chem. Soc. Rev. 41, 2283–2307.
McAndrew, C.F., Baxendale, M., 2013. Nanotechnology 24, 305202.
Nooney, R., Clifford, A., LeGuevel, X., Stranik, O., McDonagh, C., MacCraith, B.D., 2010. Anal. Bioanal. Chem. 396, 1127–1134.
Park, J.H., Choi, T.B., Kim, S.W., Hur, M.G., Yang, S.D., Yu, K.H., 2009. Radiat. Phys. Chem. 78, 623–625.
Peng, X.H., Chen, J.Y., Misewich, J.A., Wong, S.S., 2009. Chem. Soc. Rev. 38, 1076–1098.
Sharma, H., Agarwal, D.C., Shukla, A.K., Avasthi, D.K., Vankar, V.D., 2013a. J. Raman Spectrosc. 44, 12–20.
Sharma, P., Kukkar, M., Ganguli, A.K., Bhasina, A., Suri, C.R., 2013b. Analyst 138, 4312–4320.
Sun, F., Cha, H.R., Bae, K., Hong, S., Kim, J.M., Kim, S.H., Lee, J., Lee, D., 2011. Mater. Sci. Eng. A: Struct. Mater. Prop. Microstruct. Process. 528, 6636–6641.
Viet, N.X., Chikae, M., Ukita, Y., Maehashi, K., Matsumoto, K., Tamiya, E., Viet, P.H., Takamura, Y., 2013. Biosens. Bioelectron. 42, 592–597.
Wang, H.T., Dong, Z.X., Na, C.Z., 2013a. ACS Sustain. Chem. Eng. 1, 746–752.
Wang, J.L., Chen, G.H., Jiang, H., Li, Z.Y., Wang, X.M., 2013b. Analyst 138, 4427–4435.
Yick, S., Han, Z.J., Ostrikov, K., 2013. Chem. Commun. 49, 2861–2863.
Yin, P.T., Kim, T.H., Choi, J.W., Lee, K.B., 2013. Phys. Chem. Chem. Phys. 15, 12785–12799.
Yu, Y.Y., Chen, Z.G., He, S.J., Zhang, B.B., Li, X.C., Yao, M.C., 2014. Biosens. Bioelectron. 52, 147–152.
Zhang, Y.F., Xu, C.L., Li, B.X., Li, Y.B., 2013. Biosens. Bioelectron. 43, 205–210.
Zhou, H., Dong, J.H., Deo, V.K., Park, E.Y., Lee, J., 2013. Sens. Actuators B: Chem. 178, 192–199.
Zhou, H., Lee, J., Park, T.J., Lee, S.J., Park, J.Y., Lee, J., 2012. Sens. Actuators B: Chem. 163, 224–232.

Biosensors and Bioelectronics 58 (2014) 33–39

Contents lists available at ScienceDirect

Biosensors and Bioelectronics

journal homepage: www.elsevier.com/locate/bios

Metal enhanced fluorescence on nanoporous gold leaf-based assay platform for virus detection

Syed Rahin Ahmed [a,b], Md. Ashraf Hossain [b], Jung Youn Park [c], Soo-Hyung Kim [b], Dongyun Lee [d], Tetsuro Suzuki [e], Jaebeom Lee [d,*], Enoch Y. Park [a,f,**]

[a] Graduate School of Science and Technology, Shizuoka University, 836 Ohya Suruga-ku, Shizuoka 422-8529, Japan
[b] Department of Nano Fusion Technology, Pusan National University, Miryang 627-706, Republic of Korea
[c] National Fisheries Research and Development Institute, Busan 619-705, Republic of Korea
[d] Department of Nano Fusion Engineering and Cogno-Mechatronics Engineering, Pusan National University, Busan 609-735, Republic of Korea
[e] Department of Infectious Diseases, Hamamatsu University School of Medicine, 1-20-1 Higashi-ku, Handa-yama, Hamamatsu 431-3192, Japan
[f] Research Institute of Green Science and Technology, Shizuoka University, 836 Ohya Suruga-ku, Shizuoka 422-8529, Japan

ARTICLE INFO

Article history:
Received 11 October 2013
Received in revised form
26 January 2014
Accepted 15 February 2014
Available online 22 February 2014

Keywords:
Nanoporous gold leaf
Surface roughness
Fluorescence enhancement
Quantum dot
Influenza A virus

ABSTRACT

In the present study, a rapid, sensitive and quantitative detection of influenza A virus targeting hemagglutinin (HA) was developed using hybrid structure of quantum dots (QDs) and nanoporous gold leaf (NPGL). NPGL film was prepared by dealloying bimetallic film where its surface morphology and roughness were fairly controlled. Anti-influenza A virus HA antibody (ab66189) was bound with NPGL and amine ($-NH_2$) terminated QDs. These biofunctionalized NPGL and QDs formed a complex with the influenza virus A/Beijing/262/95 (H1N1) and the photoluminescence (PL) intensities of QDs were linearly correlated with the concentrations of the virus up to 1 ng/mL while no PL was observed in the absence of the virus, or in bovine serum albumin (BSA, 1 μg/mL) alone. In addition, it was demonstrated that this assay detected successfully influenza virus A/Yokohama/110/2009 (H3N2) that is isolated from a clinical sample, at a concentration of ca. 50 plaque forming units (PFU)/mL. This detection limit is 2-order more sensitive than a commercially available rapid influenza diagnostic test. From these results, the proposed assay may offer a new strategy to monitor influenza virus for public health.

1. Introduction

Epidemic diseases via transmission of the virus are becoming a threatening fear for public health system; e.g., the pandemic influenza A (H1N1) 2009 virus was firstly identified in Mexico in 2009 and caused rapid outbreaks, resulting in ca. 18,000 casualties around the world (Kawai et al., 2012; Panning et al., 2009). It continues to expand globally and causes significant rates of morbidity and mortality, particularly in the elderly and children. A rapid diagnosis of influenza viruses is vital for prevention and timely control of influenza epidemics. Currently forefront tests, i.e., immunosensors and genosensors for monitoring influenza viruses at initial stage usually require professional skill, equipment, multiple processes, and low sensitivity, resulting in retardation to clinical decision (Bonanni et al., 2010; Choi et al., 2010; Deng et al., 2011; Drexler et al., 2009; Druce et al., 2005; Egashira et al., 2008; Kok et al., 2010; Kukol et al., 2008; Owen et al., 2007; Pavlovic et al., 2008; Rahman et al., 2008; van Elden et al., 2001). Numerous technologies for higher sensitivity are emerging for virus detection.

In particular, it has been attractive to utilize photoluminescence (PL) enhancement based on the near-field plasmonic effect at metallic nanostructures (Driskell et al., 2011; Gramotnev and Bozhevolnyi, 2010; Schuller et al., 2010). The interaction between metal and semiconductor nanostructure offers attractive opportunities for tuning the optical properties of such composites based on exciton–plasmon coupling. Such composite structures feature complementary optical properties; e.g., semiconductor nanostructures give rise to high emission yields and light-harvesting capabilities, whereas the metallic surface is particularly effective for local probing, confined excitation, non-linear optics and intense PL enhancement (Achermann, 2010; Lee et al., 2006, 2007). Surface roughness has long been considered as one of the

* Corresponding author. Tel.: +82 55 350 5298; fax: +82 55 350 5299.
** Corresponding author at: Research Institute of Green Science and Technology, Shizuoka University, 836 Ohya Suruga-ku, Shizuoka 422-8529, Japan. Tel./fax: +81 54 238 4887.
E-mail addresses: rahin_sust@yahoo.com (S.R. Ahmed), ashraf3521@gmail.com (Md.A. Hossain), jypark@nfrdi.go.kr (J.Y. Park), sookim@pusan.ac.kr (S.-H. Kim), dlee@pusan.ac.kr (D. Lee), tesuzuki@hama-med.ac.jp (T. Suzuki), jaebeom@pusan.ac.kr (J. Lee), acypark@ipc.shizuoka.ac.jp, acypark@icloud.com (E.Y. Park).

http://dx.doi.org/10.1016/j.bios.2014.02.039
0956-5663

critical parameters for optimizing metal enhanced fluorescence and has enabled precise control of localized surface plasmon resonance (LSPR) as well as surface plasmon polariton (SPP). In rough metallic surface, the scattering of SPP mode can produce photons that can decrease diffraction limit and resolve the sub-wavelength structure, thereby unlocking the prospect of utilizing metal–semiconductor nanocomposite films for enhancing PL emission (Ahmed et al., 2012; Leong et al., 2010; Okamoto et al., 2004).

Nanoporous gold film has unique physical properties such as excellent stability, biocompatibility, as well as high specific surface area to form self-assembled monolayers from thiols, sulfides and disulfides (Biener et al., 2008; Huang and Sun, 2005). Usually a dealloying technique is utilized to prepare nanoporous structures with controlled pore size and ligaments. By exploiting the dealloying method, PL enhancement in the vicinity of metal nanostructures can be achieved with delicate control of the morphology of the surface on the scale of a few hundreds nanometers in conjunction with interconnected-porous structures (Ciesielski et al., 2008; Detsi et al., 2011).

In the present study, the fabrication of metallic surfaces with tunable roughness and controlled structures is reported using the dealloying method. The procedure for fabrication of metal–semiconductor hybrid nanostructures was achieved by means of self-assembly techniques, and the importance of the metallic surface morphology for PL enhancement is illustrated. Furthermore, this physical study expanded to develop a highly sensitive metal–semiconductor hybrid nanostructure for the detection of influenza virus (Fig. 1).

2. Materials and methods

2.1. Materials

3-Mercaptopropionic acid (MPA; 99%), poly-diallyldimethylammonium chloride (PDDA; M.W. 400,000–500,000), polyacrylic acid (PAA; M.W.,~450,000), cadmium perchlorate hydrate, thioglycolic acid (TGA), *N*-(3-dimethylaminopropyl)-*N*′-ethylcarbodiimide (EDC) and *N*-hydroxysuccinimide (NHS) were purchased from Sigma-Aldrich (Milwaukee, USA). Aluminum telluride (Al_2Te_3) was acquired from Cerac Company (Milwaukee, USA) at the highest purity available. The chromogenic substrate, 3,3′, 5,5′-tetramethylbenzidine (TMB) was obtained from Dojindo (Osaka, Japan). Gold leaf films were purchased from Giusto Manetti Inc. (Campi Bisenzio, Italy). Anti-Influenza A virus HA H1 antibody [B219M] (ab661189, Lot: GR40088-11), anti-Swine Influenza A (H1N1) HA antibody (ab91530, Lot: 942815), and anti-H3 (H3N2) antibody [InA227] (ab82454, Lot: GR84403-3) were purchased from Abcam Inc. (Cambridge, UK). Recombinant influenza A virus HA (H1N1) (New Caledonia/20/1999; Cat: 11683-V08H) and influenza virus A/Beijing/262/95 (H1N1) (Cat: 81N73-2) were purchased from Sino Biological Inc. (Beijing, China) and HyTest Lyd. (Turku, Finland), respectively. Influenza virus A/Yokohama/110/2009 (H3N2) that was isolated from a clinical sample was kindly provided by Dr. C. Kawakami of the Yokohama City Institute of Health, Japan, and was used for confirming the versatility of the assay system. ECL™ anti-mouse IgG, horseradish peroxidase (HRP) linked whole antibody (from sheep) was purchased from GE Healthcare UK Ltd. (Buckinghamshire, UK). All other chemicals were obtained from Wako Pure Chem. Ind. Ltd. (Osaka, Japan). All experiments were carried out using high purity deionized (DI) water (> 18 MΩ).

2.2. Preparation of NPGL and semiconductor nanoparticles

The dealloying process of NPGL film has previously been described (Ciesielski et al., 2008). In this study, a gold/silver leaf was gently placed on a microscope slide. This slide was then slowly immersed into a beaker of concentrated nitric acid in order to float the leaf at the air–acid interface. The glass slide was removed when the leaf floated freely on the surface of the nitric acid solution. Subsequently, it was dealloyed for the desired time intervals of 5, 10, 30, and 60 min, and labeled as NPGL05, NPGL10, NPGL30 and NPGL60, respectively. The leaf was removed from the acid using a glass slide and transferred into a beaker containing deionized water, where the leaf was rinsed by floating for 30 min. The dealloyed leaf was withdrawn on a glass substrate that had

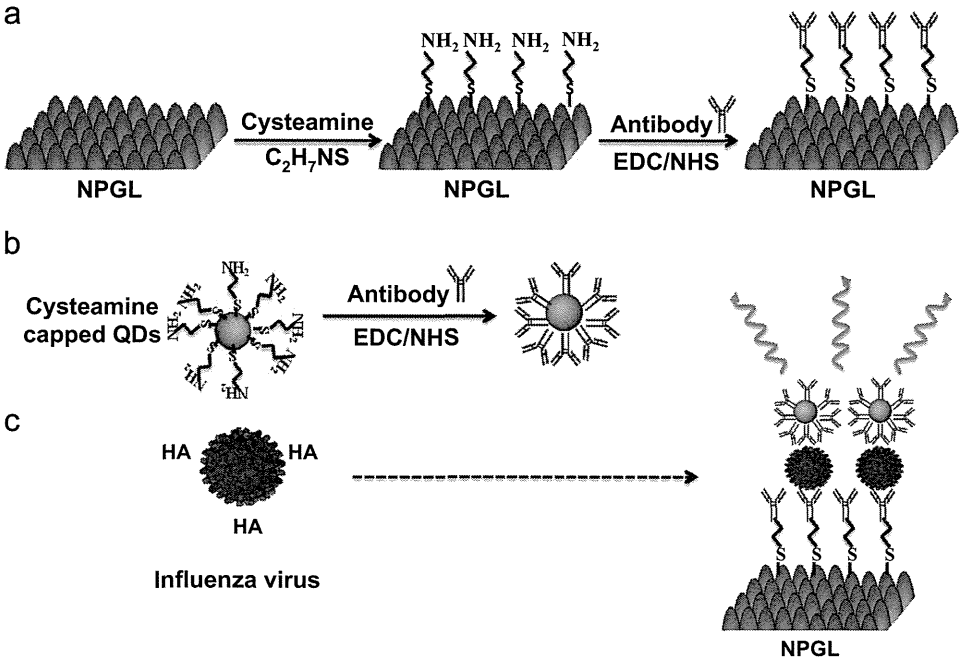

Fig. 1. Schematic of virus detection using nanoporous gold leaf (NPGL) film. The NPGL (a) and quantum dots (QDs) (b) were firstly conjugated with anti-hemagglutinin (HA) antibodies (anti-HA Ab, Y shape) by the reaction of ethylcarbodiimide (EDC)/*N*-hydroxysuccinimide (NHS). Then anti-HA Ab-conjugated with NPGL and QDs form complex (c) in presence of HA on the surface of influenza virus, finally enhancing PL intensity.

previously been modified with 3-mercaptopropyl trimethoxysilane in *n*-hexane. TGA-capped cadmium telluride (CdTe) QDs were also synthesized by a technique previously reported in detail (Gaponik et al., 2002) and stored at 4 °C prior to use.

2.3. Immobilization of CdTe QDs on the NPGL substrate

To evaluate optical properties of NPGL surface, the QDs were immobilized on the NPGL substrate by means of ultrasonic-assisted layer-by-layer (LbL) assembly (Ouyang et al., 2012; Perelshtein et al., 2008) (Supporting information S1). The polymer spacer layer of ca. 20 nm between nanocrystals and metal surface avoids unwanted quenching effects but assists PL enhancement.

2.4. Topographic observation and spectroscopic studies of NPGL films

Topographic images of the NPGL surfaces were obtained using atomic force microscopy (AFM, dilnnova, Veeco, USA) and scanning electron microscopy (SEM, S4700, Hitachi High-Technol. Co., Minato-ku, Japan).

2.5. Detection platform of HA, Influenza viruses A/Beijing/262/95 (H1N1), and A/Yokohama/110/2009 (H3N2) on NPGL

Antibody specificity for HA (H1N1) was confirmed using an enzyme-linked immunosorbent assay (ELISA) (Supporting information S2) before conjugation to NPGL5 film. The anti-HA Ab (ab66189)-conjugated NPGL5 films (Supporting information S3) were rinsed 3 times with phosphate buffered saline (PBS). 100 μl anti-HA Ab-conjugated QDs (Ab-QDs) (Supporting information S1 and S4) containing different concentrations of recombinant influenza HA (H1N1) were added to the microplate wells. An Ab-QDs solution in BSA and without influenza virus HA (H1N1) was added to the same microplate as a negative control. To determine the PL enhancement effect of NPGL05 for HA detection, an identical amount of Ab-QDs solution containing 10 mg/mL HA protein was added to the wells of microplate. The microplate was then incubated for 30 min at room temperature. An infinite® F500 microplate fluorescence reader (TECAN, Männedorf, Switzerland) was employed to measure the PL intensity of each well. The samples were excited at 380 nm, and the exciting and the emission slits were 5 and 10 nm, respectively. Based on the PL values at different concentrations of HA, a dose-dependent curve was constructed. This NPGL-based assay platform was applied on detection of two different types of influenza viruses using the same protocol as described above. Influenza virus A/Beijing/262/95 (H1N1) was detected using anti-HA (H1N1) Ab-bioconjugated NPGL and QDs; influenza virus A/Yokohama/110/2009 (H3N2) was detected using anti-HA (H3N2) Ab-bioconjugated NPGL and QDs.

2.6. Detection of influenza virus by rapid influenza diagnostic test (RIDT)

To carry out direct and complementary comparison of the detection ability with commercially available influenza diagnostic kit, a commercial RIDT (ImunoAce Flu, TAUNS Lab. Inc., Numazu, Shizuoka, Japan), was purchased to detect Influenza virus A/Yokohama/110/2009 (H3N2) according to manufacturer's protocol. Different virus titers were prepared and then, three drops of virus solution were put on the sample port of the testing kit. Positive and negative influenza diagnostic results were obtained from different significant bands that appeared on the strip paper after 10 min of incubation at room temperature.

3. Results and discussion

3.1. Topographic observation of NPGL films

SEM and AFM images showed that the pore sizes of the substrates varied depending on the dealloying times (Fig. 2a–d). The size of the pores and ligaments increased with longer dealloying times due to increased removal of the less-noble constituent (silver) of the alloy. AFM was used to evaluate the root mean

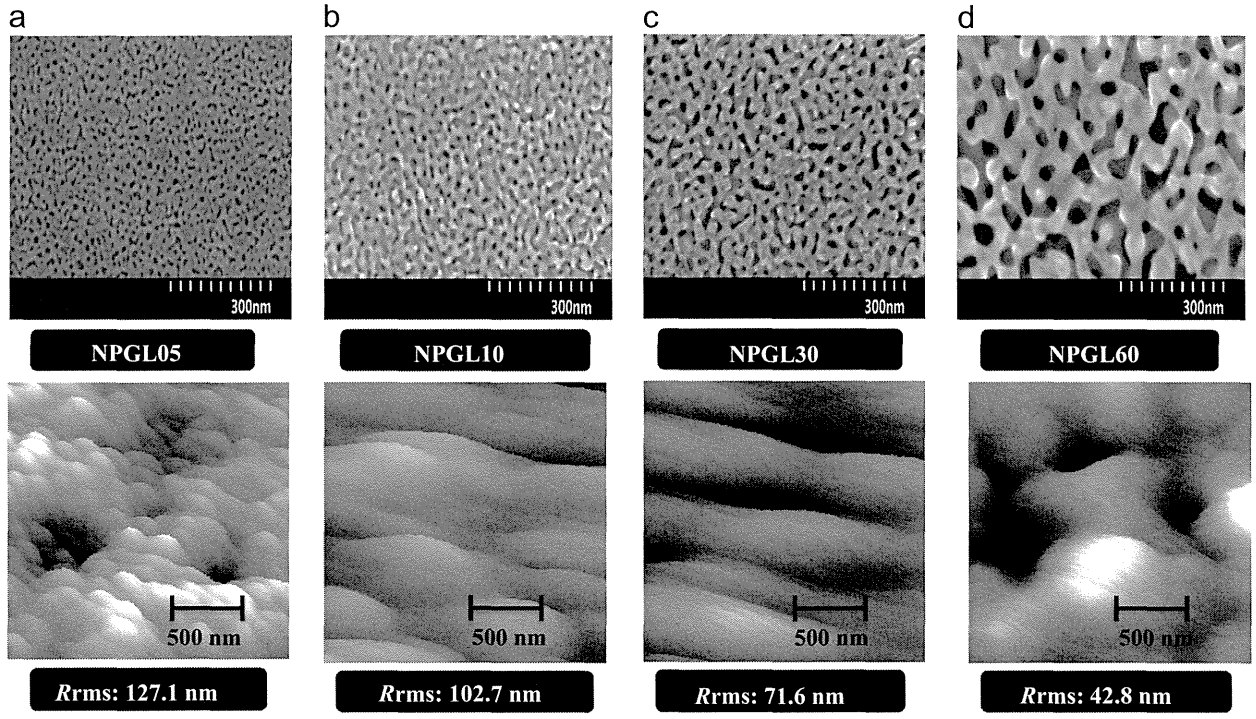

Fig. 2. SEM and AFM images and the measured R_{rms} of each NPGL sample with various dealloying times (5–60 min), where e.g., NPGL05 depicts 5 min of dealloying time. Dealloyed times are 5 min (a), 10 min (b), 30 min (c) and 60 min (d). Bars in upper and lower panels denote 300 and 500 nm respectively.

square roughness (R_{rms}) of the surface of each substrate with different dealloying times. The R_{rms} of the substrate was calculated in the scanning area ($3 \times 3\ \mu m^2$) of the AFM tip. It was found that the shorter is dealloying times the smaller is pore sizes, resulting in increasing surface irregularities and the surface roughness. Four selected NPGL samples of variant surface roughness (R_{rms} in lower panel of Fig. 2) were used for further optical evaluation.

3.2. Spectroscopic and microscopic studies of the NPGL films

The PL band of the synthesized QD solution was observed at 526 nm with a relative quantum yield of > 20% that was determined from the relative ratio versus rhodamine B dispersed in ethylene glycol, where the quantum yield of rhodamine B was 0.95 (Fig. S1A). Given that the surface roughness of each produced NPGL films differed, special care was taken in the QD immobilizing process to ensure that the equivalent amount of QDs was deposited on each substrate. Consequently, it is important to produce a monolayer of QDs on the surface of a metallic substrate. We monitored the absorbance of the QDs on the respective substrates to maintain similar intensities by adjusting the deposition time during the LbL process. Then, the PL intensity of the QD solution at the same absorption of the LbL film was measured. It was observed that the difference in the PL intensity of the various samples was less than 10%, indicating that fairly identical amount of QDs were deposited on the samples (Fig. S1B).

Indeed, PL enhancement of QDs on metal surfaces was observed. Fig. 3a shows that higher the roughness higher is the PL enhancement; e.g., the emission intensity of QDs on NPGL05 (R_{rms}=127.1 nm) and NPGL60 (R_{rms}=42.8 nm) was 9- and 2-fold higher than that on a glass substrate, respectively (Fig. 3a). When QDs were deposited on the metal surface without a spacer layer, no PL intensity was observed, rather quenching dominated. This remarkable PL enhancement may be attributed to a strong interaction with surface plasmon of metallic substrate. It has previously been reported that the excitons generated in the QDs can resonate with electron vibrations at the metal surface collectively to induce luminescence enhancement (Lee et al., 2004; Okamoto et al., 2006). Furthermore, the roughness effect on PL enhancement may be related to the multiple scattering phenomena of the SPP mode in combination with rough surfaces. Such roughness and imperfections in nanostructured random media allow SPP of high momentum to scatter and lose momentum and then couple to radioactive light (Okamoto et al., 2006). The fluorescence lifetimes (τ) of the respective samples were measured at an excitation wavelength of 380 nm using a light-emitting diode spectrophotometer (PTI Inc., USA). The spectra in Fig. 3b presents that the rougher the substrate is the shorter is the lifetime, i.e., the PL lifetime varied from 3.17 ns to 1.2 ns while the R_{rms} values varied from 42.8 to 127.1 nm (Fig. 3c). In contrast, the lifetime of CdTe QDs on glass slides was 7.42 ± 0.37 ns. In particular, the short dealloying time generated ultrafine structures that are characterized as small pores and pimples (< 10 nm) that play a major role in plasmonic scattering with consequent PL enhancement. Fig. 3d demonstrates a fluorescence microscopic image of the

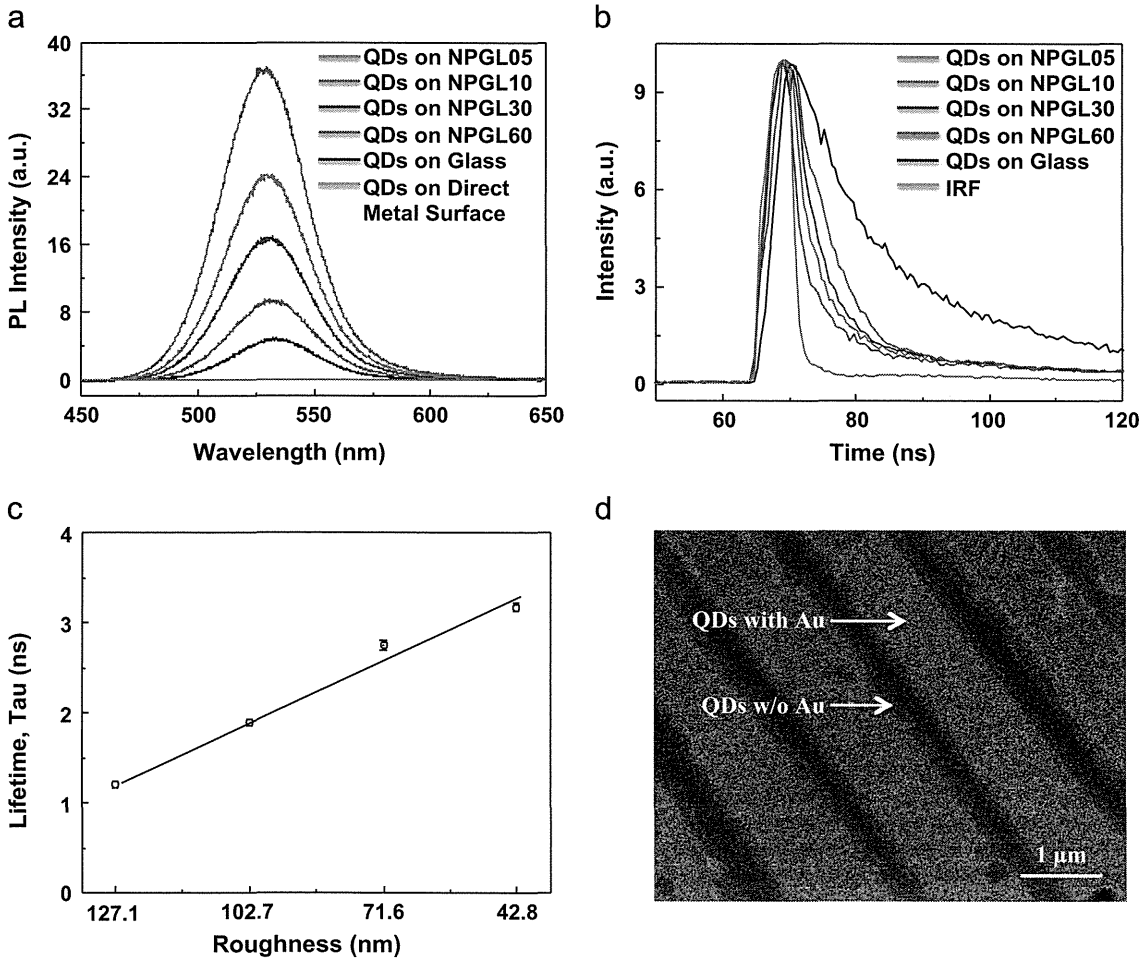

Fig. 3. (a) Photoluminescence (PL) spectra of QDs on different roughnesses of NPGL and glass substrate (for QD only); (b) time-based fluorescence kinetics profile of PL signal for QDs on different surfaces; (c) lifetimes (τ) variance depending on surface roughness; (d) fluorescence microscopic image of QDs on metallic nanostripe patterns. IRF in (b) stands for instrumental response function. The error bars in (c) indicate standard deviation (SD) in each measurement and the scale bar in (d) denotes 1 μm.

QD/polymer-deposited films on metallic nanostripe pattern to demonstrate strong PL enhancement induced by metal enhanced fluorescence. With increasing surface roughness, multiple scattering of lights occurs in nanostructured random media. The high enhancement effect observed in close proximity of metallic nanopatterns is primarily due to the absorption and/or emission bands of the QDs overlap with the scattering wavelength of the rough metallic surface. From these fundamental physical experiments NPGR05 substrate was chosen for further sensing experiments of virus detection.

3.3. Immunoassay of HA on NPGL05 and QDs

It is known that HA, a surface glycoprotein on the surface of viruses has unique immune-specificity in the initial stage of infection mechanism (Wiley and Skehel, 1987). The detailed optical observation at every respective step of bioconjugation with nanomaterials and antibodies was carefully monitored by using ELISA and FTIR spectrophotometry. Immuno-specificity of the anti-HA Ab (ab66189) for influenza virus A/Beijing/262/95 (H1N1) was investigated (Supporting information S1 and S2). A different type of Ab (ab91530) and BSA was used for comparison. A higher absorbance was observed with anti-HA Ab (ab66189) compared to the anti-HA Ab (ab91530) or BSA (Fig. S2A). From these experimental results, anti-HA Ab (ab66189) has a strong immune-specificity for influenza virus A/Beijing/262/95 (H1N1) whereas other antibody and BSA show no binding affinity with influenza A virus. The ELISA test indicated that the antibodies are successfully conjugated on the NPGLs without losing its binding affinity (Fig. S2B and C). Furthermore, FTIR bands found at 3700–3500 cm^{-1} for amide N–H stretching and 1690–1630 cm^{-1} for amide C=O stretching corresponds the chemical binding between NPGL and anti-HA Ab (ab66189) (Fig. S2D).

Then the same experiments were carried out to scrutinize any influence of binding affinity when cysteamine capped QDs were conjugated with anti-HA Ab (ab66189) using recombinant influenza H1N1 HA (New Caledonia/20/1999) (Fig. S3A), resulting that cysteamine capped QDs were successfully conjugated with the antibody (Fig. S3B and C). In fluorescence microscopic image, the aggregated and brighter spot might be virus deposited part on the film (Fig. S3D). The detection procedure consisted of three steps – (i) binding of antibody on NPGL, (ii) binding of antibody on QDs and (iii) immune-reaction between the antibody and antigen.

After confirming the binding affinity of antibody on the surface of NPGL film, the recombinant HA (H1N1) was monitored. Both NPGL film and QDs were bound with anti-HA (H1N1) Ab (ab66189). With HA, these bioconjugated components form a complex, consequently producing high PL intensity from QDs via surface plasmon resonance with the NPGL substrate. In our experiment, 3 times higher PL intensity were monitored in the nanostructure of the antibody-functionalized NPGL than that without the NPGL, where 10 μg/mL of HA was added in each experiment (Fig. 4A). In the quantitative analysis using different concentrations of HA, PL intensities were logarithmically correspondent on HA concentration in the range of 1 ng/ml–10 μg/mL (Fig. 4B and the inset). However, there was no significant PL change without any addition of HA or in the addition of BSA.

3.4. Immunoassay for virus detection

After confirmation of HA monitoring using this novel sensing system with NPGL and QDs, different concentrations of influenza virus A/Beijing/262/95 (H1N1) where the surface of this virus also has specific binding sites of anti-HA (H1N1) Ab were monitored. Similar results were observed as the previous experiment of HA only as shown in Fig. 4b. A significant PL enhancement was observed in the presence of viruses and NPGL (Fig. 5a). Furthermore, a logarithmical relationship existed between PL intensities and the virus concentration in the range of 1 ng/ml–10 μg/mL (Fig. 5b).

Using this developed monitoring system, an influenza virus A/Yokohama/110/2009 (H3N2) was monitored. The specificity of HA (H3N2) Ab 82454 for influenza virus A/Yokohama/110/2009 was confirmed (Fig. 5c), and binding of HA (H3N2) Ab 82454 with NPGL05 and QDs was also confirmed using ELISA (Fig. S4). Then, the sensitivity of influenza virus A/Yokohama/110/2009 (H3N2) detection was observed in the range of 50–10,000 plaque forming units (PFU)/mL (Fig. 5d). The detection limit was shown at ca. 50 PFU/mL.

3.5. Detection of influenza virus using rapid influenza diagnostic test (RIDT)

A commercially available RIDT kit (ImunoAce Flu, TAUNS Lab. Inc., Numazu, Shizuoka, Japan) was used for comparison with our sensing system to diagnose influenza virus infection using the influenza virus A/Yokohama/110/2009 (H3N2). Table 1 shows the results of the RIDT depending on the concentration of virus. In the case of the commercial RIDT, at least 5000 PFU/mL of virus was required for detection, which means the limit of detection (LOD) of the influenza virus detection using our sensing system of NPGL-QDs was 100 times more sensitive than that of the commercial RIDT (Fig. S5).

In this study, a new detection method on metallic surface based on exciton–plasmon interaction was presented. In particular, the

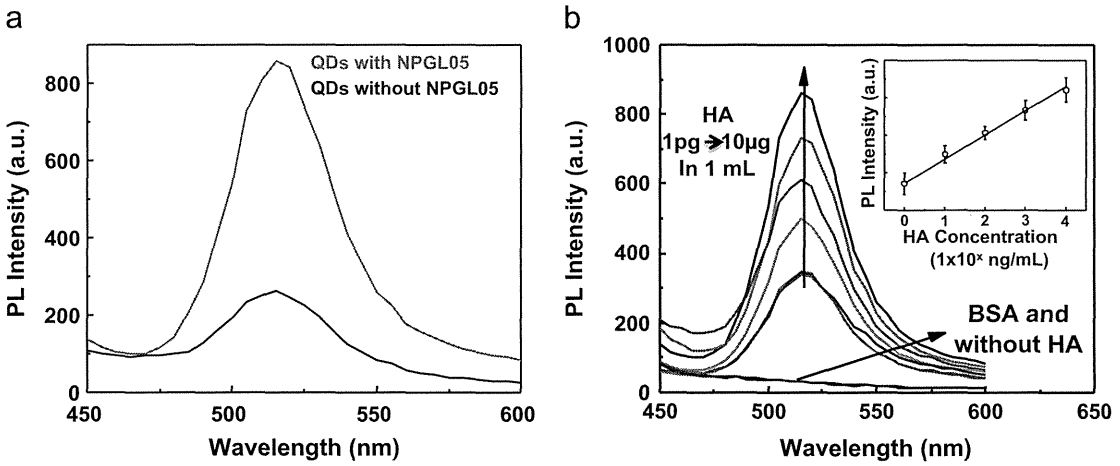

Fig. 4. (a) PL enhancement of QDs with and without the nanostructure; (b) PL enhancement corresponding on different quantities of recombinant influenza HA (H1N1) on anti-HA Ab-conjugated NPGL05. (Inset) The calibration curve of PL intensity versus HA concentration. The error bars indicate SD in each measurement.

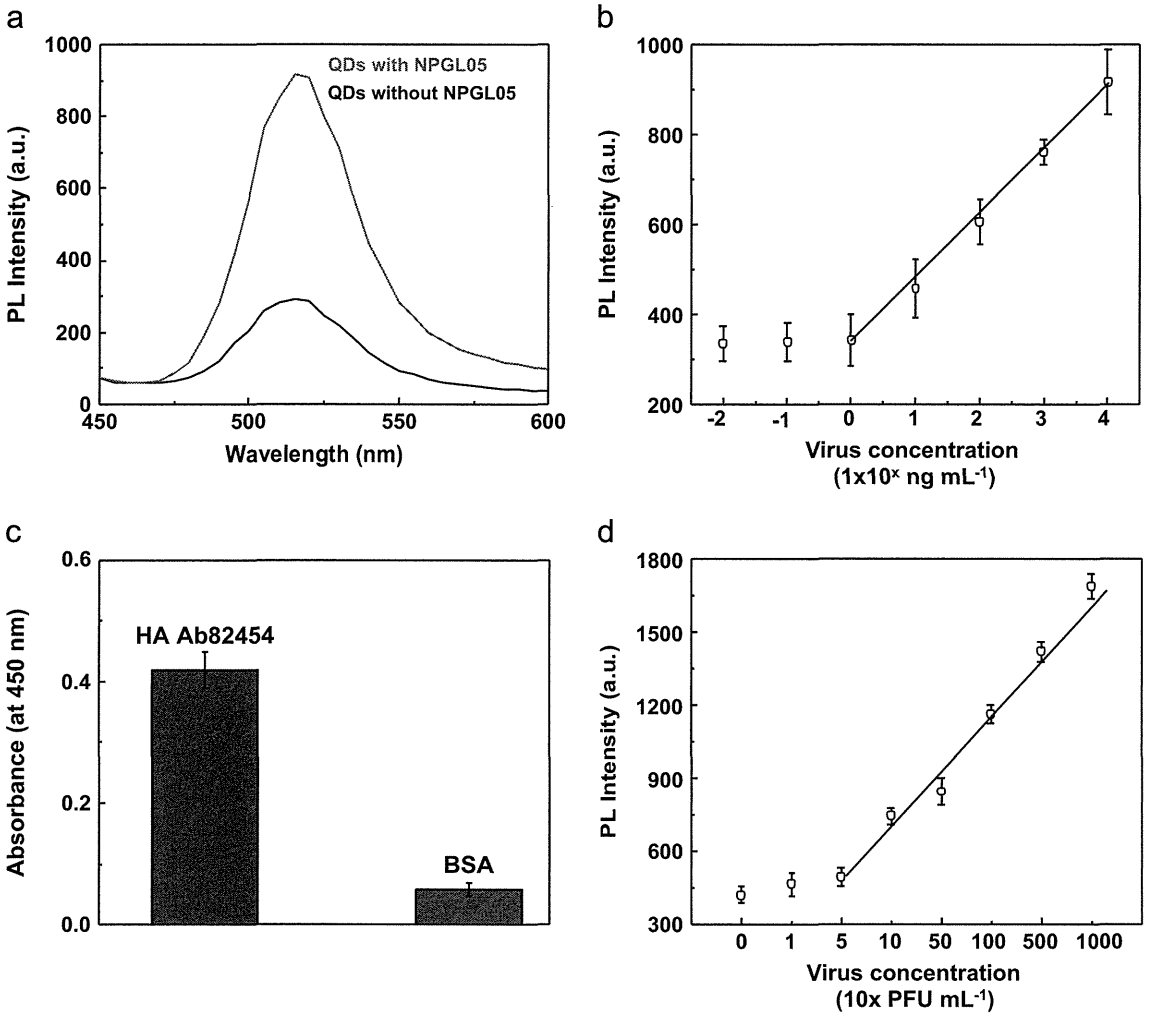

Fig. 5. (a) PL spectroscopic detection of influenza virus A/Beijing/262/95 (H1N1) using anti-HA (H1N1) Ab (ab66189)-bioconjugated QDs depending on the existence of anti-HA (H1N1) Ab (ab66189)-bioconjugated NPGL05 film; (b) PL intensity versus influenza virus A/Beijing/262/95 (H1N1) concentration; (c) ELISA results for anti-HA (H3N2) Ab 82454 binding with influenza virus A/Yokohama/110/2009 (H3N2); (d) the calibration curve of PL intensity corresponding on the concentration of the influenza virus A/Yokohama/110/2009 (H3N2). The error bars in (B–D) indicate SD ($n=3$).

Table 1
Comparison of influenza virus A/Yokohama/110/2009 (H3N2) detection using RIDT.

Detection method	Virus concentration (PFU/mL)								
	10,000	5000	1000	500	100	50	10	1	0
This study	+	+	+	+	+	+	−	−	−
Commercial RIDT	+	+	−	−	−	−	−	−	−

Note: + and − denote the positive and negative diagnoses, respectively.

research centered on the development of robust rough metallic surfaces that would be used for the generation of high efficient optical device for biosensor applications. Many implications for medical take care require a low detection system. An important goal here was to improve detection limit with high sensitivity. As we can see, our proposed detection method showed at least 100 times higher sensitivity than a representative commercial test kit. It might result from the presence of plasmonic rough metallic surface and adjacent control of distance between QDs to induce PL enhancement. In addition, the assay is performed with fewer amounts of reagents and easier to wash out unbound reagents. However, because of the lack of many medical samples, the huge analysis is not attainable using our technique up to now, which will be included in future work.

4. Conclusion

This paper reports a near-field optical evaluation of QDs and plasmonic surface composites with varying roughness. A dramatic enhancement of PL intensity and decay rate of the QDs was achieved on rougher metallic surfaces. The observation of these PL enhancements from nanocomposites was further applied for the development of sensitive influenza virus A (H1N1) detection (up to 1 ng/mL) and influenza A (H3N2) virus isolated from a clinical sample (up to 50 PFU/mL). The proposed method represented an alternative traditional method by requiring a higher sensitivity, much smaller sample volume, less amount reagents. Further research will be focused on the development of rough plasmonic metallic surface using self-assembly techniques as well as clinical evaluation.

Acknowledgments

We thank to Dr. Chiharu Kawakami of the Yokohama City Institute of Health, Japan, for providing influenza virus A/Yokohama/110/2009 (H3N2). This study was supported by a grant from the Korea Healthcare Technology R&D Project (A110191), the Ministry for Health, Welfare & Family Affairs, Republic of Korea;

by the National Fisheries Research & Development Institute (RP-2012-BT-030); by the Civil & Military Technology Cooperation Program through the National Research Foundation of Korea (NRF) funded by the Ministry of Science, ICT & Future Planning (No. 2013M3C1A9055407); and by the Financial Supporting Project of Long-term Overseas Dispatch of PNU's Tenure-track Faculty, 2011. This work was supported partly by Promotion of Nanobio-Technology Research to support Aging and Welfare Society from the Ministry of Education, Culture, Sports, Science and Technology, Japan. There was no additional external funding received for this study.

Appendix. Supporting information

Supplementary data associated with this article can be found in the online version at http://dx.doi.org/10.1016/j.bios.2014.02.039.

References

Achermann, M., 2010. J. Phys. Chem. Lett. 1, 2837–2843.
Ahmed, S.R., Cha, H.R., Park, J.Y., Park, E.Y., Lee, D., Lee, J., 2012. Nanoscale Res. Lett. 7, 438.
Biener, J., Nyce, G.W., Hodge, A.M., Biener, M.M., Hamza, A.V., Maier, S.A., 2008. Adv. Mater. 20, 1211–1217.
Bonanni, A., Pividori, M.I., del Valle, M., 2010. Analyst 135, 1765–1772.
Choi, Y.J., Kim, H.J., Park, J.S., Oh, M.H., Nam, H.S., Kim, Y.B., Cho, B.K., Ji, M.J., Oh, J.S., 2010. J. Clin. Microbiol. 48, 2260–2262.
Ciesielski, P.N., Scott, A.M., Faulkner, C.J., Berron, B.J., Cliffel, D.E., Jennings, G.K., 2008. ACS Nano 2, 2465–2472.
Deng, Y.M., Caldwell, N., Barr, I.G., 2011. PLoS One 6, e23400.
Detsi, E., Schootbrugge, M., Punzhin, S., Onck, P.R., Hosson, J.T.M.D., 2011. Scr. Mater. 64, 319–322.
Drexler, J.F., Helmer, A., Kirberg, H., Reber, U., Panning, M., Müller, M., Höfling, K., Matz, B., Drosten, C., Eis-Hübinger, A.M., 2009. Emerg. Infect. Dis. 15, 1662–1664.
Driskell, J.D., Jones, C.A., Tompkins, S.M., Tripp, R.A., 2011. Analyst 136, 3083–3090.
Druce, J., Tran, T., Kelly, H., Kaye, M., Chibo, D., Kostecki, R., Amiri, A., Catton, M., Birch, C., 2005. J. Med. Virol. 75, 122–129.
Egashira, N., Morita, S., Hifumi, E., Mitoma, Y., Uda, T., 2008. Anal. Chem. 80, 4020–4025.
Gaponik, N., Talapin, D.V., Rogach, A.L., Hoppe, K., Shevchenko, E.V., Kornowski, A., Eychmüller, A., Weller, H., 2002. J. Phys. Chem. B 106, 7177–7185.
Gramotnev, D.K., Bozhevolnyi, S.I., 2010. Nat. Photonics 4, 83–91.
Huang, J.F., Sun, I.W., 2005. Adv. Funct. Mater. 15, 989–994.
Kawai, Y., Kimura, Y., Lezhava, A., Kanamori, H., Usui, K., Hanami, T., Soma, T., Morlighem, J.E., Saga, S., Ishizu, Y., Aoki, S., Endo, R., Oguchi-Katayama, A., Kogo, Y., Mitani, Y., Ishidao, T., Kawakami, C., Kurata, H., Furuya, Y., Satito, Y., Okazaki, N., Chikahira, M., Hayashi, E., Tsuruoka, S., Toguchi, T., Saito, Y., Ban, T., Izumi, S., Uryu, H., Kudo, K., Sakai-Tagawa, Y., Kawaoka, Y., Hirai, A., Hayashizaki, Y., Ishikawa, T., 2012. PLoS One 7, e30236.
Kok, J., Blyth, C.C., Foo, H., Patterson, J., Taylor, J., McPhie, K., Ratnamohan, V.M., Iredell, J.R., Dwyer, D.E., 2010. J. Clin. Microbiol. 48, 290–291.
Kukol, A., Li, P., Estrela, P., Ko-Ferrigno, P., Migliorato, P., 2008. Anal. Biochem. 374, 143–153.
Lee, J., Govorov, A.X., Dulka, J., Kotov, N.A., 2004. Nano Lett. 4, 2323–2330.
Lee, J., Hernandez, P., Lee, J., Govorov, A.O., Kotov, N.A., 2007. Nat. Mater. 6, 291–295.
Lee, J., Javed, T., Skeini, T., Govorov, A.O., Bryant, G.W., Kotov, N.A., 2006. Angew. Chem. Int. Ed. 45, 4819–4823.
Leong, K., Chen, Y., Masiello, D.J., Zin, M.T., Hnilova, M., Ma, H., Tamerler, C., Sarikaya, M., Ginger, D.S., Jen, A.K.Y., 2010. Adv. Funct. Mater. 20, 2675–2682.
Okamoto, K., Vyawahare, S., Scherer, A., 2006. J. Opt. Soc. Am. B 23, 1674–1678.
Okamoto, K., Niki, I., Shvartser, A., Narukawa, Y., Mukai, T., Scherer, A., 2004. Nat. Mater. 3, 601–605.
Ouyang, J., Chang, M., Zhang, Y., Li, X., 2012. Thin Solid Films 520, 2994–2999.
Owen, T.W., Al-Kaysi, R.O., Bardeen, C.J., Cheng, Q., 2007. Sens. Actuators B – Chem. 126, 691–699.
Panning, M., Eickmann, M., Landt, O., Monazahian, M., Ölschläger, S., Baumgarte, S., Reischl, U., Wenzel, J.J., Niller, H.H., Günther, S., 2009. Eurosurveillance 14, 2003–2008.
Pavlovic, E., Lai, R.Y., Wu, T.T., Ferguson, B.S., Sun, R., Plaxco, K.W., Soh, H.T., 2008. Langmuir 24, 1102–1107.
Perelshtein, I., Applerot, G., Perkas, N., Guibert, G., Mikhailov, S., Gedanken, A., 2008. Nanotechnology 19, 245705–245710.
Rahman, M., Vandermause, M.F., Kieke, B.A., Belongia, E.A., 2008. Diagn. Microbiol. Infect. Dis. 62, 162–166.
Schuller, J.A., Barnard, E.S., Cai, W., Jun, Y.C., White, J.S., Brongersma, M.L., 2010. Nat. Mater. 9, 193–204.
van Elden, L.J., van Essen, G.A., Boucher, C.A., van Loon, A.M., Nijhuis, M., Schipper, P., Verheij, T.J., Hoepelman, I.M., 2001. Br. J. Gen. Pract. 51, 630–634.
Wiley, D.C., Skehel, J.J., 1987. Ann. Rev. Biochem. 56, 365–394.

IPS-1 Is Essential for Type III IFN Production by Hepatocytes and Dendritic Cells in Response to Hepatitis C Virus Infection

Masaaki Okamoto,* Hiroyuki Oshiumi,* Masahiro Azuma,* Nobuyuki Kato,† Misako Matsumoto,* and Tsukasa Seya*

Hepatitis C virus (HCV) is a major cause of liver disease. The innate immune system is essential for controlling HCV replication, and HCV is recognized by RIG-I and TLR3, which evoke innate immune responses through IPS-1 and TICAM-1 adaptor molecules, respectively. IL-28B is a type III IFN, and genetic polymorphisms upstream of its gene are strongly associated with the efficacy of polyethylene glycol–IFN and ribavirin therapy. As seen with type I IFNs, type III IFNs induce antiviral responses to HCV. Recent studies established the essential role of TLR3–TICAM-1 pathway in type III IFN production in response to HCV infection. Contrary to previous studies, we revealed an essential role of IPS-1 in type III IFN production in response to HCV. First, using IPS-1 knockout mice, we revealed that IPS-1 was essential for type III IFN production by mouse hepatocytes and $CD8^+$ dendritic cells (DCs) in response to cytoplasmic HCV RNA. Second, we demonstrated that type III IFN induced RIG-I but not TLR3 expression in $CD8^+$ DCs and augmented type III IFN production in response to cytoplasmic HCV RNA. Moreover, we showed that type III IFN induced cytoplasmic antiviral protein expression in DCs and hepatocytes but failed to promote DC-mediated NK cell activation or cross-priming. Our study indicated that IPS-1–dependent pathway plays a crucial role in type III IFN production by $CD8^+$ DCs and hepatocytes in response to HCV, leading to cytoplasmic antiviral protein expressions. ***The Journal of Immunology*****, 2014, 192: 2770–2777.**

Hepatitis C virus (HCV) is a major cause of chronic liver disease (1). The 3′ untranslated region (UTR) of the HCV genome is recognized by a cytoplasmic viral RNA sensor RIG-I (2). HCV RNA induces RIG-I–dependent type I IFN production to promote hepatic immune responses in vivo (2). RIG-I is a member of RIG-I–like receptors (RLRs), which include MDA5 and LGP2. RLRs trigger signal that induces type I IFN and other inflammatory cytokines through the IPS-1 adaptor molecule (3). RLRs are localized in the cytoplasm and recognize cytoplasmic dsRNAs. Another pattern recognition receptor, TLR3, recognizes dsRNAs within early endosomes or on cell surfaces (4). Human monocyte-derived dendritic cells (DCs) require TLR3 to recognize HCV RNA in vitro (5), and TLR3 induces type I IFN production through the TICAM-1 adaptor, also called Toll/IL-1R domain-containing adapter inducing IFN-β (6, 7).

*Department of Microbiology and Immunology, Hokkaido University Graduate School of Medicine, Sapporo 060-8638, Japan; and †Department of Tumor Virology, Okayama University Graduate School of Medicine, Dentistry, and Pharmaceutical Science, Okayama 700-8558, Japan

Received for publication June 3, 2013. Accepted for publication January 13, 2014.

This work was supported in part by a grant-in-aid from the Ministry of Education, Science, and Culture of Japan, the Ministry of Health, Labour, and Welfare of Japan, and the Kato Memorial Bioscience Foundation.

Address correspondence and reprint requests to Dr. Hiroyuki Oshiumi and Dr. Tsukasa Seya, Department of Microbiology and Immunology, Graduate School of Medicine, Hokkaido University, Kita-15, Nishi-7, Kita-ku Sapporo 060-8638, Japan. E-mail addresses: oshiumi@med.hokudai.ac.jp (H.O.) and seya-tu@pop.med.hokudai.ac.jp (T.S.)

The online version of this article contains supplemental material.

Abbreviations used in this article: BM-DC, bone marrow–derived dendritic cell; BM-Mf, bone marrow–derived macrophage; DC, dendritic cell; HCV, hepatitis C virus; KO, knockout; Mf, macrophage; Oc, O cured; RLR, RIG-I–like receptor; UTR, untranslated region.

www.jimmunol.org/cgi/doi/10.4049/jimmunol.1301459

IL-28B is a type III IFN (also called IFN-λ), which includes IL-28A (IFN-λ2) and IL-29 (IFN-λ1) (8). Type III IFNs interacts with heterodimeric receptors that consist of IL-10Rβ and IL-28Rα subunits (8). Polymorphisms upstream of the IL-28B (IFN-λ3) gene are significantly associated with the responses to polyethylene glycol–IFN and ribavirin in patients with chronic genotype 1 HCV infections (9–12). As seen with type I IFNs, type III IFNs have antiviral activities against HCV (13). Type I IFNs induce the expression of IFN-inducible genes, which have antiviral activities, and can promote cross-priming and NK cell activation (14). However, the roles of type III IFN in cross-priming and NK cell activation are largely unknown, and the functional differences between type I and III IFN are uncertain.

Mouse $CD8^+$ DCs and its human counterpart $BDCA3^+$ DCs are the major producers of type III IFNs in response to polyI:C (15). $CD8^+$ DCs highly express TLR3 and have strong cross-priming capability (16). A recent study showed that TLR3 was important for type III IFN production by $BDCA3^+$ DCs in response to cell-cultured HCV (17). RIG-I efficiently recognizes the 3′ UTR of the HCV RNA genome, and, thus, RIG-I adaptor IPS-1 is essential for type I IFN production (2). However, the role of an IPS-1–dependent pathway in type III IFN production in vivo has been underestimated. In this study, we investigated the role of an IPS-1–dependent pathway in type III IFN production in vivo and in vitro using IPS-1 knockout (KO) mice and established an essential role of IPS-1 in type III IFN production in response to HCV RNA. Our study indicated that not only TICAM-1 but also IPS-1 are essential for type III IFN production in response to HCV.

Materials and Methods

Mice

All mice were backcrossed with C57BL/6 mice more than seven times before use. The generation of TICAM-1 and IPS-1 KO mice was described

previously (18). All mice were maintained under specific pathogen-free conditions in the Animal Facility of the Hokkaido University Graduate School of Medicine (Sapporo, Japan). Animal experiments were conducted according to the guidelines established by the Animal Safety Center, Japan.

Cell lines and reagents

Human hepatocyte cell lines O cells and O cured (Oc) cells that contained HCV 1b replicons were provided by N. Kato (Okayama University). Mouse hepatocyte cell line was described previously (19). PolyI:C was purchased from GE Healthcare and dissolved in saline. An OVA ($H2K^b$-SL8) tetramer was purchased from MBL. PE-CD80, -CD86, -NK1.1, FITC-CD8, and allophycocyanin-CD3e Abs were purchased from BioLegend, and PE-CD40, FITC-CD69, and allophycocyanin-CD11c Abs were from eBioscience. An ELISA kit for IFN-β was purchased from PBL Biomedical Laboratories, and ELISA kits for mouse IL-28 (IFN-λ2/3) were purchased from Abcam and eBioscience. An ELISA kit for mouse IFN-γ was purchased from eBioscience. ELISA was performed according to the manufacturer's instructions. Mouse IFN-α and IFN-λ3 (IL-28B) were purchased from Miltenyi Biotec and R&D Systems, respectively.

Cell preparation

Spleen $CD8^+$ and $CD4^+$ DCs were isolated using $CD8^+$ DC isolation kit and CD4-positive isolation kit, according to manufacturer's instruction (Miltenyi Biotec). Spleen $CD11c^+$ DCs were isolated using CD11c microbeads. To obtain splenic double-negative (DN) DCs, $CD4^+$ and $CD8^+$ cells were depleted from mouse spleen cells using CD4 and CD8 MicroBeads (Miltenyi Biotec), and then $CD11c^+$ DCs were positively selected using CD11c MicroBeads (Miltenyi Biotec). We confirmed that >90% of isolated cells were $CD4^-$, $CD8^-$, and $CD11c^+$ DCs. Splenic NK cells were isolated using mouse DX5 MicroBeads (Miltenyi Biotec). The cells were analyzed by flow cytometry on a FACSCalibur instrument (BD Biosciences), followed by data analysis using FlowJo software.

Generation of bone marrow–derived DCs and bone marrow–derived macrophages

Bone marrow cells were prepared from the femur and tibia. The cells were cultured in RPMI 1640 medium with 10% FCS, 100 μM 2-ME, and 10 ng/ml murine GM-CSF or culture supernatant of L929 expressing M-CSF. Medium was changed every 2 d. Six days after isolation, cells were collected.

Hydrodynamic injection

Total RNA from the human hepatocyte cell lines O cells and Oc cells was extracted using TRIzol reagent (Invitrogen). HCV genotype 1b 3′ UTR RNA, including the polyU/UC region, was synthesized using T7 and SP6 RNA polymerase and purified with TRIzol, as described previously (20). RNA was i.v. injected into a mouse by a hydrodynamic method using a TransIT Hydrodynamic Gene Delivery System (Takara), according to the manufacturer's instruction.

Quantitative PCR

For quantitative PCR, total RNA was extracted using TRIzol reagent (Invitrogen), after which 0.1–1 μg RNA was reverse transcribed using a high-capacity cDNA transcription kit with an RNase inhibitor kit (Applied Biosystems), according to the manufacturer's instructions. Quantitative PCR was performed using a Step One real-time PCR system (Applied Biosystems). The expression of cytokine mRNA was normalized to that of β-actin mRNA, and the fold increase was determined by dividing the expressions in each sample by that of wild type at 0 h. PCR primers for mouse IFN-λ amplified both IFN-λ2 and λ3 mRNA. The primer sequences are described in Supplemental Table 1.

Activation of NK cells in vitro

NK cells and $CD11c^+$ DCs were isolated from spleens using DX5 and CD11c MicroBeads (Miltenyi Biotec), respectively. A total of 2×10^5 NK

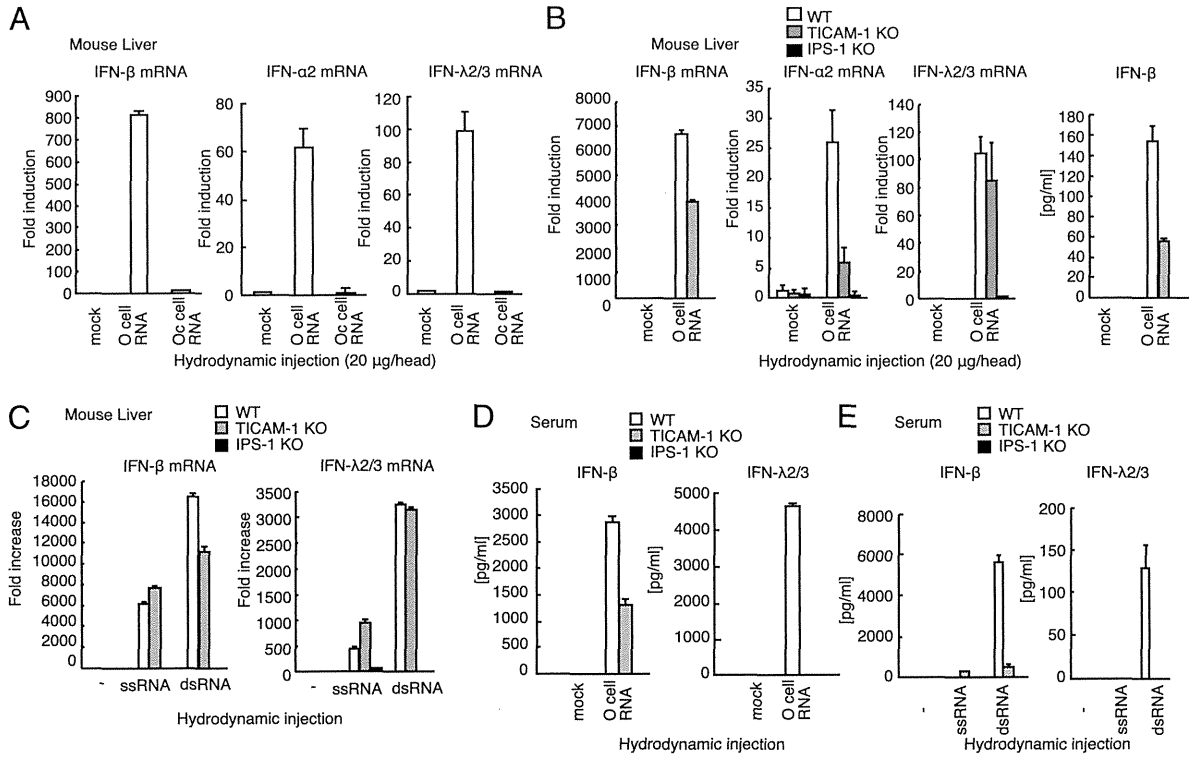

FIGURE 1. Type I and type III IFN productions in response to HCV RNA in vivo. (**A**) O cell and Oc cell RNA (20 μg) were hydrodynamically injected into wild-type mice. Six hours later, mouse livers were excised, and IFN-β, α2, and -λ2/3 mRNA levels were determined by quantitative RT-PCR. (**B**) O cell RNA (20 μg) with HCV replicons was hydrodynamically injected into wild-type, TICAM-1 KO, and IPS-1 KO mice. Six hours after injection, IFN-β, α2, and -λ2/3 mRNA levels in liver were determined by quantitative RT-PCR. IFN-β protein levels in mouse livers were determined by ELISA. (**C**) HCV ssRNA or HCV dsRNA (5 μg) was hydrodynamically injected into wild-type, TICAM-1 KO, and IPS-1 KO mice. Six hours after injection, IFN-β and -λ2/3 mRNA levels in liver were determined by quantitative RT-PCR. (**D**) O cell RNA (20 μg) with HCV replicons was hydrodynamically injected into wild-type, TICAM-1 KO, and IPS-1 KO mice. Six hours after injection, serum IFN-β and -λ2/3 concentrations were determined by ELISA. (**E**) HCV ssRNA or HCV dsRNA (5 μg) was hydrodynamically injected into wild-type, TICAM-1 KO, and IPS-1 KO mice. Six hours after injection, serum IFN-β and -λ2/3 concentrations were determined by ELISA.

cells and 1×10^5 DCs was cocultured with IFN-λ, IFN-α, or polyI:C. After 6, 12, and 24 h, IFN-γ concentrations in the supernatants were determined by ELISA. To determine CD69 expression, $NK1.1^+$ and $CD3e^+$ cells in 24-h sample were gated.

Ag-specific T cell expansion in vivo

OVA (1 mg) and IFN-λ (0.5 μg) or 1×10^5 IU IFN-α were i.p. injected into mice on day 0, and then 0.5 μg IFN-λ or 1×10^5 IU of IFN-α was injected into mice on days 1, 2, and 4. On day 7, spleens were homogenized and stained with FITC CD8α Ab and PE-OVA tetramer for detecting OVA (SL8)-specific $CD8^+$ T cell population. For a negative control, PBS in place of IFN was injected on days 0, 1, 2, and 4. For a positive control, 100 μg polyI:C and OVA were injected into mice on day 0.

Results

TICAM-1 is essential for type III IFN production in response to polyI:C

DCs require the TLR3 adaptor TICAM-1 to produce type III IFN in response to polyI:C (15). Adding polyI:C to culture medium for mouse bone marrow–derived macrophages (BM-Mf) induced IFN-β, IFN-α2, IFN-α4, and IFN-λ2/3 mRNA expression, and TICAM-1 KO abolished IFN-λ2/3 mRNA expression (Supplemental Fig. 1A). These results suggested an essential role for TICAM-1 in type III IFN expression by BM-Mf.

Next, we examined cytokine mRNA expression in mouse tissues in response to i.p. injected polyI:C. IFN-β, IFN-α2, and IFN-α4 mRNA expression was detectable in both wild-type and TICAM-1 KO mice livers, whereas IFN-λ2/3 mRNA expression was not detected in TICAM-1 KO mouse liver (Supplemental Fig. 1B–1E). A recent study showed that TLR3 KO abolished IFN-λ serum levels in response to i.v. polyI:C injection (15). Our results and those in the previous study confirmed that TICAM-1 is essential for type III IFN expression in response to polyI:C.

IPS-1 plays a crucial role in type III IFN production in response to HCV in vivo

IPS-1 is essential for type I IFN production in response to HCV RNA and polyI:C in vivo (2, 3). We investigated whether IPS-1 could induce type III IFN production. An ectopic expression study using IPS-1 and TICAM-1 expression vectors showed that both TICAM-1 and IPS-1 activated the IFN-λ1 promoter (Supplemental Fig. 2A, 2B), which suggested that IPS-1 has the ability to induce IFN-λ1 expression. A deletion analysis showed that a 150- to 556-aa region of TICAM-1 and the transmembrane region of IPS-1 were essential for IFN-β, -λ1, and 2/3 promoter activations (Supplemental Fig. 2C, 2D).

Hydrodynamic injection is a highly efficient procedure to deliver nucleic acids to the mouse liver (21), and Gale Jr. and colleagues

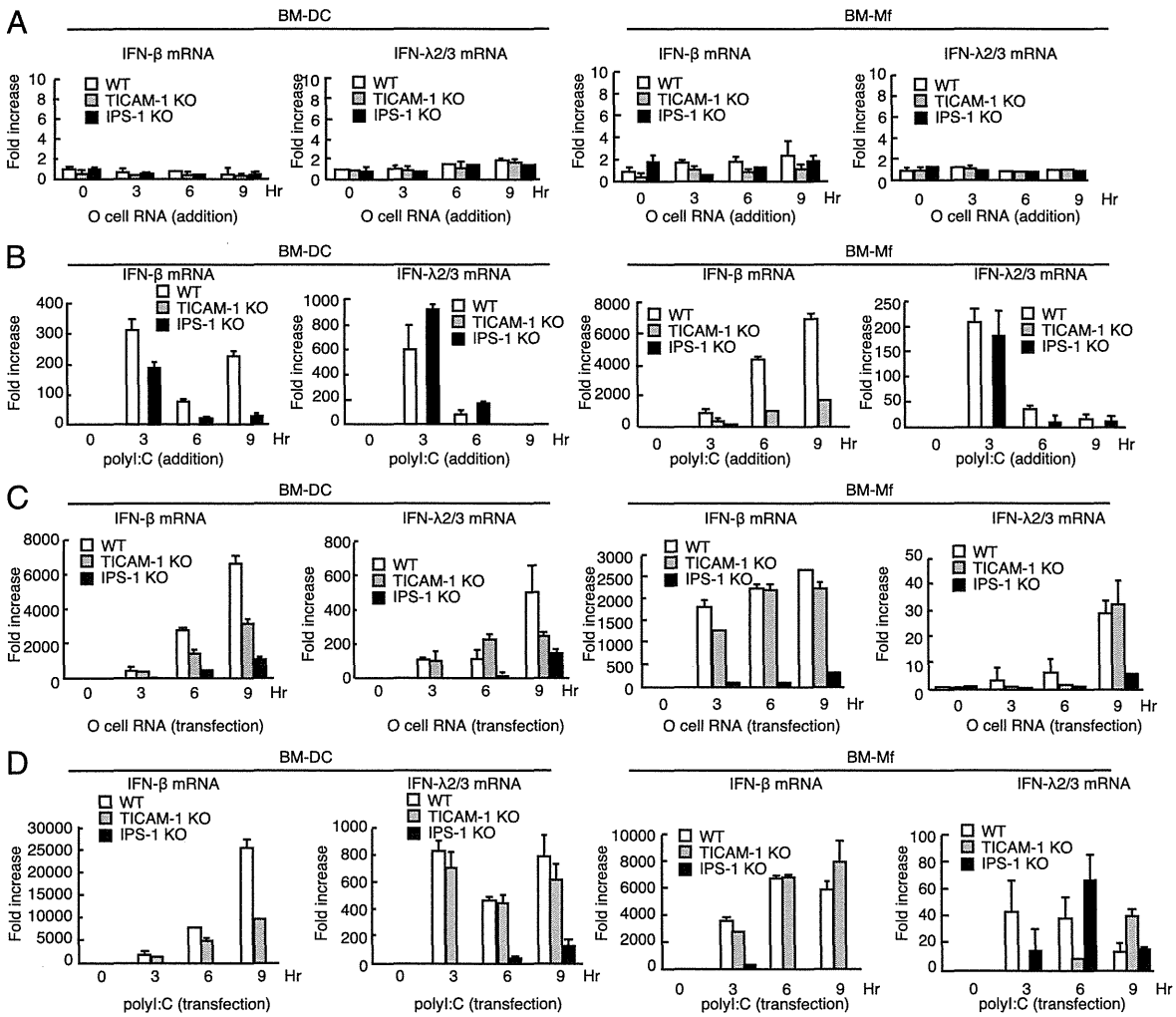

FIGURE 2. Type I and type III IFN expression in mouse DCs and Mfs in response to HCV RNA. (**A** and **B**) O cell RNA (A) or polyI:C (B) (20 μg) was added to the culture medium of BM-DCs and BM-Mfs derived from wild-type, TICAM-1 KO, and IPS-1 KO mice. IFN-β and IFN-λ2/3 mRNA levels were determined by quantitative RT-PCR at indicated hours. (**C** and **D**) O cell RNA (C) or polyI:C (D) (1 μg) was transfected into BM-DCs and BM-Mfs derived from wild-type, TICAM-1 KO, or IPS-1 KO mice. IFN-β (C) and -λ2/3 (D) mRNA levels were determined by quantitative RT-PCR.

(2) previously used a hydrodynamic assay to assess the role of RIG-I in type I IFN production in response to HCV RNA in vivo. Thus, to investigate the response to HCV RNA in vivo, we also used a hydrodynamic assay. We used RNA extracted from hepatocyte cell lines, O cells and Oc cells. O cells are derived from HuH-7 cells and contain HCV 1b full-length replicons (22). Oc cells were obtained by eliminating these replicons using IFN-α treatment (22). RNAs extracted from O cells (with HCV RNA) and Oc cells (without HCV RNA) were hydrodynamically injected into mouse livers, after which the cytokine expressions in mouse livers were determined. In wild-type mouse liver, O cell but not Oc cell RNA induced IFN-α2, β, and λ mRNA expression (Fig. 1A), which indicated that these cytokines were expressed in response to HCV RNAs within O cells that contained the HCV genome and replication intermediates in hepatocyte. Knockout of IPS-1 severely reduced IFN-β and α2 mRNA expressions in mouse liver in response to hydrodynamically injected O cell RNA (Fig. 1B). IFN-β protein level in mouse liver was also reduced by IPS-1 knockout (Fig. 1B). Although TICAM-1 was essential for IFN-λ2/3 mRNA expression in liver in response to i.p. injected polyI:C (Supplemental Fig. 1), TICAM-1 was dispensable for IFN-λ2/3 mRNA expression in response to hydrodynamically injected O cell RNA (Fig. 1B). In contrast, IPS-1 was essential for IFN-λ2/3 mRNA expression in response to hydrodynamically injected O cell RNA (Fig. 1B). A requirement for IPS-1 for IFN-λ2/3 mRNA expression in the liver was also found when in vitro synthesized HCV dsRNAs and ssRNAs were used for the hydrodynamic assay (Fig. 1C). These results suggested that IPS-1 plays a crucial role in type III IFN production in response to HCV RNA in vivo.

To corroborate the role of IPS-1 in type III IFN production, we next measured serum IFN-λ and -β levels in response to hydrodynamic injection of O cell RNA, HCV ssRNA, and HCV dsRNA. Interestingly, IPS-1 KO markedly reduced serum IFN-λ2/3 levels (Fig. 1D, 1E). Unexpectedly, TICAM-1 KO also reduced serum IFN-λ levels (Fig. 1D, 1E). Because TICAM-1 was dispensable for IFN-λ mRNA expression in the liver, it is possible that serum IFN-λ was produced from DCs in other tissues in a TICAM-1–dependent manner, as described below. Our data indicated that both TICAM-1 and IPS-1 are essential for type III IFN in response to HCV RNA in vivo. When polyI:C was hydrodynamically injected, knockout of TICAM-1 or IPS-1 moderately reduced IFN-λ2/3 levels in sera (Supplemental Fig. 3).

DCs produce type III IFN through an IPS-1–dependent pathway in response to cytoplasmic HCV RNA

HCV proteins and minus strands of its genome are detected in DCs and macrophages (Mfs) of chronically HCV-infected patients (23, 24), and recent study showed that DCs produce type I and III IFNs in response to HCV (17, 25). Thus, we assessed the role of IPS-1 in type III IFN production by DCs and Mfs in response to HCV RNA. Surprisingly, adding O cell RNA into the culture medium did not induce any IFN-β and -λ2/3 mRNA expression (Fig. 2A), whereas adding polyI:C into culture medium efficiently induced IFN-β and -λ2/3 mRNA expression (Fig. 2B), and TICAM-1 KO abolished the IFN-λ2/3 mRNA expression in bone marrow–derived DCs (BM-DCs) and BM-Mfs (Fig. 2B). It has been shown that polyI:C is preferentially internalized and activates TLR3 in human monocyte-derived DCs, whereas in vitro transcribed viral dsRNA hardly induced IFN-β production in monocyte-derived DCs (26). Thus, there is a possibility that, unlike polyI:C, TLR3 ligand in O cell RNA was not delivered to endosome where TLR3 is localized. Next, cells were stimulated with O cell RNA or polyI:C by transfection. BM-DCs and BM-Mfs expressed IFN-β and -λ2/3

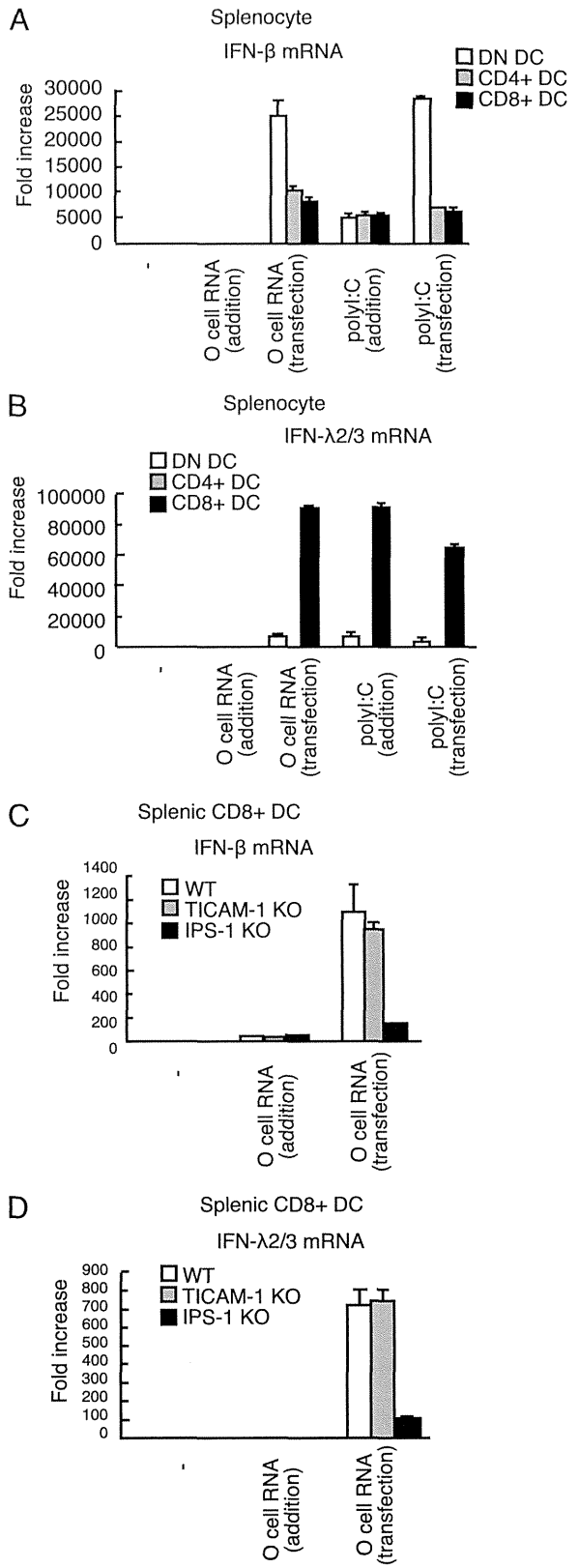

FIGURE 3. Type III IFN production by $CD8^+$ DCs. (**A** and **B**) $CD4^+$, $CD8^+$, and DN DCs were isolated from mouse spleens and stimulated with 20 μg O cell RNA without transfection or stimulated with 1 μg O cell RNA by transfection for 6 h. IFN-β (A) and -λ2/3 (B) mRNA levels were determined by quantitative RT-PCR. (**C** and **D**) $CD8^+$ DCs were isolated from wild-type, TICAM-1 KO, or IPS-1 KO mouse spleens. O cell RNA (20 μg) was added to the culture medium, or 1 μg O cell RNA was transfected into $CD8^+$ DCs. Six hours after transfection, IFN-β (C) and -λ2/3 (D) mRNA levels were determined by quantitative RT-PCR.

mRNAs in response to O cell RNA and polyI:C (Fig. 2C, 2D). IPS-1 KO severely reduced IFN-λ2/3 mRNA expression in BM-DCs and BM-Mfs in response to O cell RNA (Fig. 2C). These results indicated that IPS-1 in BM-DCs and BM-Mfs plays a crucial role in IFN-λ2/3 mRNA expression in response to cytoplasmic HCV RNA.

Mice have $CD4^+$, $CD8^+$, and DN DCs. Thus, we next examined the IFN-β and -λ2/3 mRNA expression in these mouse DC subsets. As seen with BM-DCs, the mouse DCs expressed IFN-β and -λ2/3 mRNA in response to polyI:C but not O cell RNA in the culture medium, whereas stimulation with polyI:C or O cell RNA by transfection strongly induced their expression (Fig. 3A, 3B). Interestingly, $CD8^+$ DCs highly expressed IFN-λ2/3 mRNA in response to stimulation with polyI:C or O cell RNA by transfection compared with $CD4^+$ and DN DCs (Fig. 3A, 3B), and IPS-1 KO but not TICAM-1 KO severely reduced IFN-λ2/3 expression in $CD8^+$ DCs in response to O cell RNA transfection (Fig. 3C, 3D). This indicated that IPS-1 was essential for IFN-λ2/3 mRNA expression in $CD8^+$ DCs in response to cytoplasmic HCV RNA.

It was recently reported that exosomes mediate cell-to-cell transfer of HCV RNA from infected cells to cocultured DCs (27). We examined the production of IFN-β and -λ2/3 by $CD8^+$ DCs that were cocultured with O cells and Oc cells. Coculture with O cells but not Oc cells induced IFN-β and -λ2/3 production by $CD8^+$ DCs (Fig. 4A, 4B). Interestingly, TICAM-1 KO abolished IFN-λ2/3 mRNA expression and protein production, whereas IPS-1 KO failed to reduce IFN-λ2/3 mRNA expression and protein production in $CD8^+$ DCs (Fig. 4C, 4D). This suggested that TICAM-1 but not IPS-1 was essential for IFN-λ2/3 production by $CD8^+$ DCs when cocultured with hepatocytes with HCV replicons.

Type III IFN increases RIG-I expression in $CD8^+$ DC

The receptor for type III IFN consists of IL-10RB and IL-28Rα subunits (8). DN and $CD4^+$ DCs and NK cells did not express IL-28Rα mRNA, whereas $CD8^+$ DCs expressed both IL-10RB and IL-28Rα mRNAs (Fig. 5A). Thus, we investigated the effects of IFN-λ on DC function.

First, we examined DC cell surface markers. Unlike IFN-α, IFN-λ3 hardly increased CD40, 80, and 86 surface marker expressions on $CD8^+$ DCs (Fig. 5B). Second, we examined the effects of IFN-λ3 on cross-priming because $CD8^+$ DCs have high cross-priming capability. OVA, IFN-α, and/or IFN-λ3 were i.p. injected into mice according to the indicated schedules (Fig. 5C). Seven days after injection, OVA (SL8)-specific $CD8^+$ T cells in spleens were quantified by tetramer staining. For a positive control, OVA and polyI:C were i.p. injected into mice. The results showed that IFN-λ3 failed to increase OVA-specific $CD8^+$ T cells in the spleens and suggested that IFN-λ3 failed to promote cross-priming at least in our experimental condition (Fig. 5C).

Third, we examined NK cell activation by DCs. NK cells and DCs were isolated from mouse spleens and were cocultured for 24 h in the presence of IFN-α, λ3, or polyI:C. Although IFN-γ production was increased by IFN-α stimulation, IFN-λ3 failed to increase IFN-γ production (Fig. 5D). Next, we investigated a cell surface marker for NK cells when cocultured with DCs. The expression of CD69, a NK cell activation marker, was not increased by IFN-λ3 stimulation (Fig. 5E). These results indicated that, unlike IFN-α, IFN-λ3 failed to enhance the activation of NK cells by DCs.

Fourth, we investigated the expression of antiviral genes in $CD8^+$ DCs in response to IFN-λ3 stimulation. Interestingly, IFN-λ3 stimulation increased RIG-I and Mx1 but not TLR3 mRNA expression in $CD8^+$ DCs (Fig. 6A). In addition, pretreatment with IFN-λ3 augmented IFN-λ2/3 mRNA expression in $CD8^+$ DCs in response to HCV RNA (Fig. 6B). Taken together, type III IFN induced RIG-I and antiviral protein expression but failed to promote DC-mediated NK cell activation and cross-priming.

Hepatocytes express type III IFN receptors. Thus, we examined the effects of IFN-λ on mouse hepatocytes. As with IFN-α, IFN-λ3 stimulation induced both TLR3 and RIG-I mRNA expression in mouse hepatocyte (Fig. 6C). Antiviral nucleases, ISG20 and RNaseL, and an IFN-inducible gene, Mx1, were induced by IFN-λ3 or IFN-α treatment (Fig. 6C). Pretreating mouse hepatocytes with IFN-λ3 enhanced IFN-β and -λ2/3 mRNA expression in response to stimulation with HCV RNA by transfection (Fig. 6D). These results indicated that IFN-λ3 induced cytoplasmic antivirus protein expression in mouse hepatocytes. We confirmed that IFN-λ3 treatment significantly reduced HCV RNA levels in O cells with HCV replicons (Fig. 6E). A previous study also reported that IFN-λ inhibits HCV replication (13).

Discussion

Previous studies have established the importance of the TLR3 pathway for type III IFN production in response to polyI:C (15) or HCV (17). In this study, we established the importance of IPS-1–dependent pathway for type III IFN production in response to cytoplasmic HCV RNA in vivo and in vitro using a mouse model. These data indicated that there are at least two main pathways for type III IFN production in vivo, as follows: one is TICAM-1 dependent, and the other is IPS-1 dependent.

We revealed that IFN-λ was efficiently produced by $CD8^+$ DCs, the mouse counterpart of human $BDCA3^+$ DCs, in response to

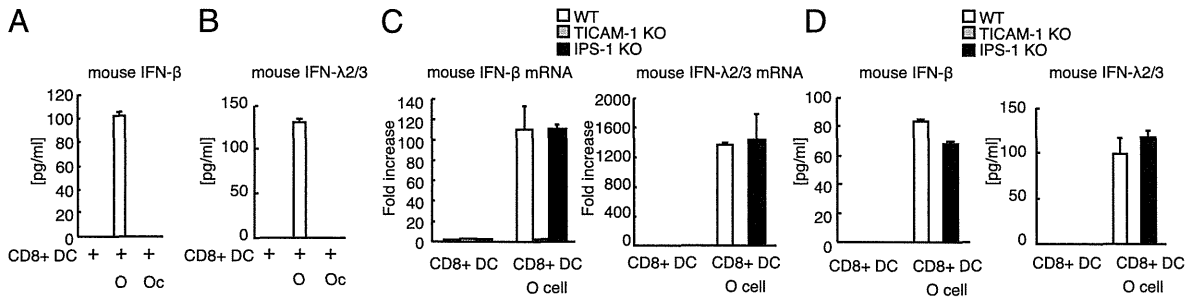

FIGURE 4. IFN-β and -λ production by $CD8^+$ DCs cocultured with hepatocytes with HCV replicons. (**A** and **B**) $CD8^+$ DCs isolated from wild-type spleens were cocultured with O cells (with HCV replicons) or Oc cells (without HCV replicons). After 24 h of coculture, IFN-β (A) and -λ2/3 (B) concentrations in culture medium were determined by ELISA. (**C**) $CD8^+$ DCs isolated from wild-type, TICAM-1 KO, or IPS-1 KO spleens were cocultured with O cells with HCV replicons for six hours, and then IFN-β and -λ2/3 mRNA expression was determined by RT-qPCR. (**D**) $CD8^+$ DCs isolated from wild-type, TICAM-1 KO, or IPS-1 KO spleens were cocultured with O cells with HCV replicons. IFN-β and -λ2/3 concentrations in culture medium were determined by ELISA.

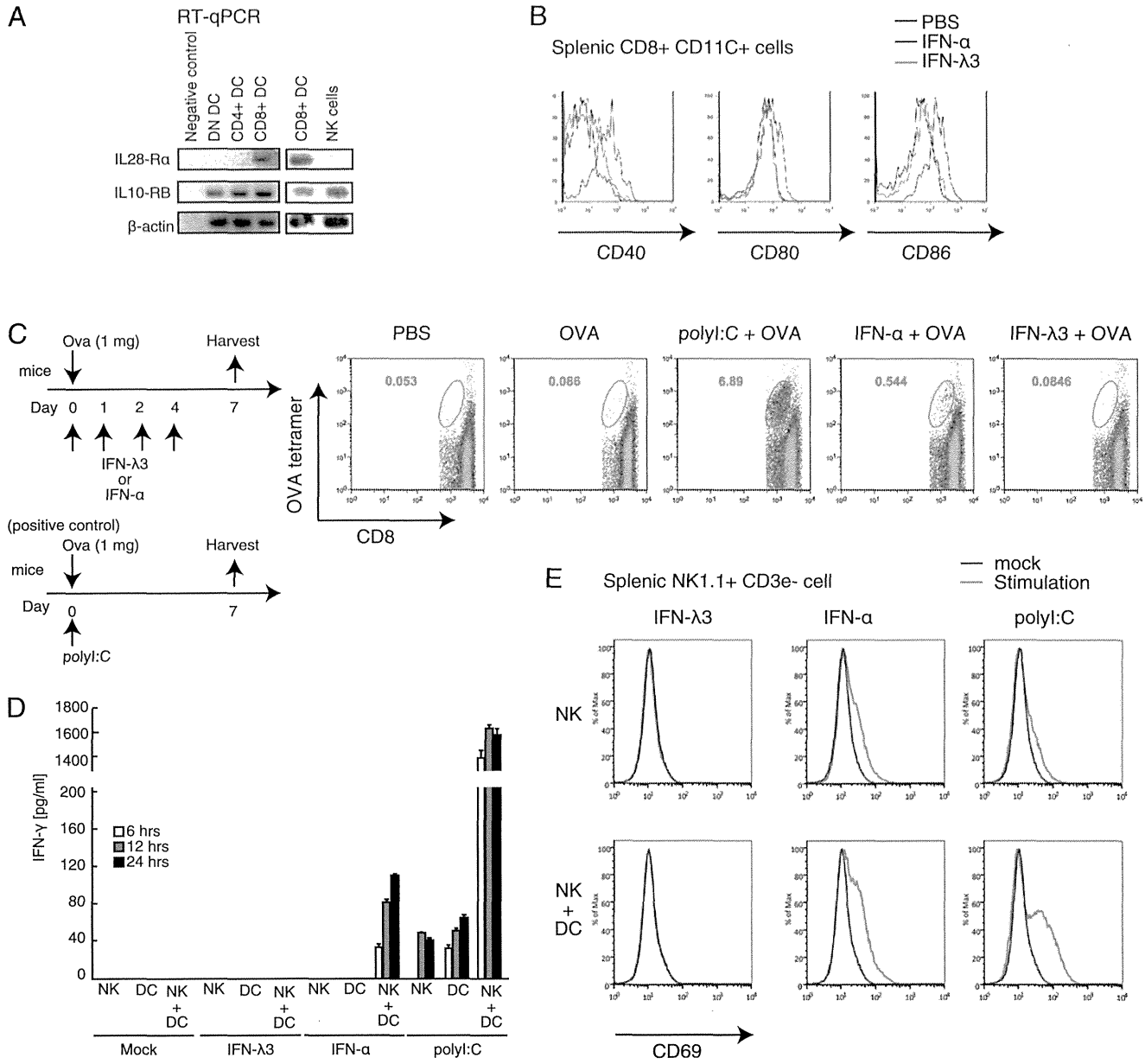

FIGURE 5. IFN-λ effects on DC functions. (**A**) DN, $CD4^+$, $CD8^+$ DCs, and NK cells were isolated from wild-type mouse spleens. IL-28Rα and IL-10RB mRNA were determined by RT-PCR. (**B**) A total of 0.5 μg IFN-λ3 or 1×10^5 IU IFN-α was i.p. injected into mice. Six hours after injection, spleen $CD8^+$ DCs were isolated, and cell surface expressions of CD40, 80, and 86 were determined by FACS analysis. (**C**) OVA and IFN-λ or IFN-α were i.p. injected into mice on day 0, and then IFN-λ or IFN-α was injected into mice on days 1, 2, and 4. Spleens were excised on day 7, and OVA (SL8)-specific $CD8^+$ T cells were determined by a tetramer assay. For a negative control, PBS in place of IFN was injected on days 0, 1, 2, and 4. For a positive control, polyI:C and OVA were injected into mice on day 0. (**D**) NK cells and $CD11c^+$ DCs were isolated from mouse spleens and then stimulated with 1000 U/ml IFN-α, 100 ng/ml IFN-λ3, or 100 μg/ml polyI:C. IFN-γ concentrations in the culture medium at the indicated times were determined by ELISA. (**E**) NK cells were isolated from mouse spleens and then cultured with or without spleen $CD11c^+$ DCs. Cells were stimulated with 1000 U/ml IFN-α, 100 ng/ml IFN-λ3, or 20 μg polyI:C. CD69 expression on NK cells was determined by FACS analysis.

cytoplasmic HCV RNA. Moreover, our data showed that IFN-λ stimulation increased the mRNA expression of RIG-I but not that of TLR3 in $CD8^+$ DCs, and $CD8^+$ DCs required IPS-1 to produce IFN-λ in response to stimulation with cytoplasmic HCV RNA. Furthermore, IFN-λ enhanced the mRNA expression of IFN-λ itself in $CD8^+$ DCs, which suggested a positive feedback loop for IFN-λ mRNA expression in $CD8^+$ DCs. IFN-λ failed to promote DC-mediated NK activation or cross-priming at least in our experimental conditions, whereas antiviral proteins, such as ISG20 and RNaseL, were efficiently induced by IFN-λ stimulation in hepatocytes and $CD8^+$ DCs. These results established a novel role of IPS-1 in innate immune response against HCV via IFN-λ production. IFN-λ pretreatment markedly increased IFN-β mRNA expression in response to HCV RNAs in mouse hepatocyte but not in $CD8^+$ DCs (Fig. 6B, 6D). Although the underlying mechanism is unclear, it is possible that there is a cell-type–specific role of IFN-λ.

It was recently reported that $BDCA3^+$ DCs require TLR3 for type III IFN production in response to cell-cultured HCV (17). They used a HCV 2a JFH1 strain that cannot infect human DCs in vitro (5). We also showed that the TLR3 adaptor TICAM-1 was essential for type III IFN production by $CD8^+$ DCs when cocultured with O cells with HCV replicons. Thus, TLR3 appears to be essential for type III IFN production by DCs that are not infected with HCV. It